EUROPEAN ORGANIZATION FOR NUCLEAR RESEARCH

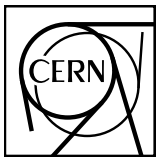

CERN-EP-2022-231
28 October 2022

Spin Density Matrix Elements in Exclusive ρ^0 Meson Muoproduction

The COMPASS Collaboration

Abstract

We report on a measurement of Spin Density Matrix Elements (SDMEs) in hard exclusive ρ^0 meson muoproduction at COMPASS using 160 GeV/c polarised μ^+ and μ^- beams impinging on a liquid hydrogen target. The measurement covers the kinematic range 5.0 GeV/c^2 < W < 17.0 GeV/c^2, 1.0 (GeV/c)^2 < Q^2 < 10.0 (GeV/c)^2 and 0.01 (GeV/c)^2 < p_{T}^2 < 0.5 (GeV/c)^2. Here, W denotes the mass of the final hadronic system, Q^2 the virtuality of the exchanged photon, and p_{T} the transverse momentum of the ρ^0 meson with respect to the virtual-photon direction. The measured non-zero SDMEs for the transitions of transversely polarised virtual photons to longitudinally polarised vector mesons ($\gamma_T^* \to V_L$) indicate a violation of s-channel helicity conservation. Additionally, we observe a dominant contribution of natural-parity-exchange transitions and a very small contribution of unnatural-parity-exchange transitions, which is compatible with zero within experimental uncertainties. The results provide important input for modelling Generalised Parton Distributions (GPDs). In particular, they may allow one to evaluate in a model-dependent way the role of parton helicity-flip GPDs in exclusive ρ^0 production.

(to be submitted to Eur. Phys. J. C)

1 Introduction

Exclusive vector meson production in lepton-nucleon scattering provides a convenient tool for studying the production mechanism and, in a model-dependent way, the structure of the nucleon. In this paper, exclusive ρ^0 meson muoproduction on the proton is studied:

$$\mu + p \rightarrow \mu' + p' + \rho^0. \tag{1}$$

In the one-photon-exchange approximation, this process is described by the interaction of a virtual photon γ^* with the target proton p:

$$\gamma^* + p \rightarrow p' + \rho^0. \tag{2}$$

At high virtuality Q^2 of the photon, this process is known as Hard Exclusive Meson Production (HEMP). A wealth of information is contained in the spin density matrix elements (SDMEs), which are the observables describing how the spin components of the virtual photon are transferred to those of the created vector meson [1, 2]. The comparison of the new ρ^0 results presented in this paper to our previous ω results [31] will provide insight into details of their respective production mechanism, because ρ^0 and ω vector mesons have different quantum numbers and hence different quark-flavour and gluon contributions to the cross section.

The colour dipole model describes HEMP as a fluctuation of the virtual photon into a quark-antiquark ($q\bar{q}$) pair that scatters off the nucleon and then hadronises into the final vector meson [3]. Regge phenomenology and perturbative QCD (pQCD) provide complementary approaches to describe the scattering of the $q\bar{q}$ pair off the nucleon. The interaction of the $q\bar{q}$ pair with the nucleon depends on the transverse separation between q and $\bar{q}$. A pair with large transverse separation is thought to interact primarily softly, which is described in Regge phenomenology [4] by the exchange of a pomeron or a secondary reggeon. The interaction of a $q\bar{q}$ pair with small transverse separation is calculable in pQCD. In lowest order of the strong coupling constant α_s, this hard interaction is mediated by the exchange of a gluon-gluon or quark-antiquark system. In this approach, it is possible to calculate not only transitions without spin-flip induced by both longitudinally (L) and transversely (T) polarised virtual photons, $\gamma^*_L \rightarrow \rho^0_L$ and $\gamma^*_T \rightarrow \rho^0_T$, but also to estimate single and double spin-flip transitions.

In an alternative approach, the framework of General Parton Distributions (GPDs) [5–9] can be used to describe HEMP. These distribution functions contain a wealth of new information on the parton structure of the nucleon. For HEMP by longitudinally polarised virtual photons, the amplitude was proven to factorise into a hard-scattering part and a soft part [8, 10]. While the former is calculable in pQCD, the latter contains GPDs that describe the structure of the probed nucleon and a distribution amplitude that accounts for the structure of the produced meson. This factorisation is referred to as collinear because parton transverse momenta are neglected. For HEMP by transversely polarised virtual photons no similar proof of factorisation exists. Instead, phenomenological pQCD-inspired models [11–14] postulate the so-called $k_\perp$ factorisation, where $k_\perp$ denotes parton transverse momentum. In particular, the Goloskokov-Kroll (GK) model [12–16] allows for a simultaneous description of SDMEs as well as target and beam-spin asymmetries for HEMP induced by both longitudinally and transversely polarised virtual photons.

The chiral-even GPDs H^f and E^f are used to describe at leading twist the production of longitudinally polarised vector mesons by longitudinally polarised virtual photons. Here, f denotes a quark of a given flavour or a gluon. In the GK model, the chiral-odd GPDs H^f_T and $\bar{E}^f_T$ are used together with higher-twist effects in the three-dimensional light-cone wave function to describe $\gamma^*_T \rightarrow \rho^0_L$ transitions. These GPDs account for a helicity flip of the "active" quark and are hence related to the violation of s-channel helicity conservation (SCHC). The GPDs $\widetilde{H}^f$ and $\widetilde{E}^f$, and also the pion-pole exchange mechanism treated in the GK model as one-boson exchange contribution, provide unnatural parity (UPE) contributions to the transitions $\gamma^*_T \rightarrow \rho^0_T$ and $\gamma^*_L \rightarrow \rho^0_T$. With this ansatz the GK model offers an explanation for the

contrast between a substantial UPE contribution in exclusive ω production and a small UPE contribution in exclusive ρ^0 production.

Spin density matrix elements are related to helicity amplitudes that describe transitions between specified spin states of virtual photon, target proton, produced vector meson, and recoil proton. In the case of an unpolarised nucleon target, SDMEs depend only on the helicities of virtual photon and produced meson, if the initial and final spin states of the proton are summed over. The interpretation of the measured SDME values is a rich field and in this paper we will address the following: the test of SCHC, the evaluation of UPE contributions, the determination of the phase difference between helicity amplitudes, and the calculation of the longitudinal-to-transverse cross-section ratio.

There exist numerous measurements of hard exclusive ρ^0 production in lepton scattering off hydrogen, deuterium and ^{3}He targets. At small values of W, measurements were performed at CORNELL [17] and by CLAS [18, 19]. For intermediate values of W, results were obtained by HERMES [20–22], NMC [23] and Fermilab experiment E665 [24]. At highest values of W, results were obtained by the H1 [25, 26] and ZEUS [27–29] Collaborations.

However, among the quoted publications only three [22, 25, 28] are providing extensive sets of SDME values that were obtained through an analysis of three-dimensional angular distributions of ρ^0 production and decay. Such an analysis allows the determination of all 15 SDMEs that are not coupled to the beam polarisation ("unpolarised SDMEs"), as in Refs. [25, 28]. The complete set of 23 SDMEs, which includes the 8 SDMEs coupled to the beam polarisation ("polarised SDMEs"), was obtained for the first time by HERMES [22]. The published results confirm the dominance of amplitudes for NPE transitions and the violation of the SCHC hypothesis that is observed for the transitions $\gamma^*_T \to \rho^0_L$.

The present COMPASS results on SDMEs for exclusive ρ^0 muoproduction have the potential to further constrain GPDs, in particular in conjunction with the published COMPASS results on SDMEs for exclusive ω production [31]. These additional constraints on GPD parameterisations are beyond those obtained from measurements of cross sections and spin asymmetries in HEMP. The COMPASS SDME results provide input to asses the role of chiral-odd, i.e., parton helicity-flip GPDs in exclusive vector-meson production, which are related to the mechanism of SCHC violation.

2 Theoretical formalism

Throughout this article, the theoretical formalism of SDMEs and helicity amplitudes introduced by K. Schilling and G. Wolf [1] is used, thereby following the notation from Refs. [31, 32].

2.1 Definition of Spin Density Matrix Elements

In the hard exclusive process of vector-meson production on a nucleon N with helicity λ_N (λ'_N) in the initial (final) state (Eq. 2), the transition of a virtual photon γ^* with helicity λ_γ to a vector meson V with helicity λ_V is described by helicity amplitudes $F_{\lambda_V \lambda'_N \lambda_\gamma \lambda_N}$, which depend on the three kinematic variables W, Q^2, and t' with $t' \equiv |t| - t_0 \approx p_\mathrm{T}^2$. Here t is the squared four-momentum transfer to the proton, t_0 represents the smallest kinematically allowed value of $|t|$ for given Q^2 and meson mass and p_T^2 the squared transverse momentum of the vector meson with respect to the virtual-photon direction. In the γ^*-N centre-of-mass (CM) system, the vector-meson spin density matrix $\rho_{\lambda_V \lambda'_V}$ is related to the helicity amplitude $F_{\lambda_V \lambda'_N \lambda_\gamma \lambda_N}$ as [1]

$$\rho_{\lambda_V \lambda'_V} = \frac{1}{2\mathcal{N}} \sum_{\lambda_\gamma \lambda'_\gamma \lambda_N \lambda'_N} F_{\lambda_V \lambda'_N \lambda_\gamma \lambda_N} \, \varrho^{U+L}_{\lambda_\gamma \lambda'_\gamma} \, F^*_{\lambda'_V \lambda'_N \lambda'_\gamma \lambda_N}, \tag{3}$$

with the normalisation factor $\mathcal{N}$ [1, 22]. The virtual-photon spin density matrix $\varrho^{U+L}_{\lambda_\gamma \lambda'_\gamma}$ [22] describes the QED-calculable sub-process $\mu \to \mu' + \gamma^*$. It can be decomposed into elements coupled to the longitudinal

beam polarisation P_b (indicated by a superscript L) and elements not coupled to P_b (superscript U):

$$\varrho^{U+L}_{\lambda_\gamma\lambda'_\gamma} = \varrho^{U}_{\lambda_\gamma\lambda'_\gamma} + P_\mathrm{b}\ \varrho^{L}_{\lambda_\gamma\lambda'_\gamma}. \tag{4}$$

The vector-meson spin density matrix elements (SDMEs) discussed below are related to either U or L elements in Eq. 4 and will correspondingly be referred to as "unpolarised" or "polarised" in the following.

After the decomposition of $\varrho^{U+L}_{\lambda_\gamma\lambda'_\gamma}$ into the set of 3×3 Hermitian matrices [1], the vector-meson spin density matrix can be expressed in terms of a set of nine matrices $\rho^{\alpha}_{\lambda_V\lambda'_V}$ corresponding to different virtual-photon polarisation states. Here α= 0 corresponds to unpolarised transverse photons, α= 1, 2 to the two directions of linear polarisation, α = 3 to circular photons and α = 4 represents longitudinal virtual photons. The terms with α = 5 ... 8 correspond to the interference of transverse and longitudinal amplitudes.

Lacking the possibility to separate contributions from longitudinally and transversely polarised virtual photons, as is the case for this experiment, one usually defines SDMEs as follows:

$$r^{04}_{\lambda_V\lambda'_V} = (\rho^{0}_{\lambda_V\lambda'_V} + \epsilon R\rho^{4}_{\lambda_V\lambda'_V})(1+\epsilon R)^{-1},$$

$$r^{\alpha}_{\lambda_V\lambda'_V} = \begin{cases} \rho^{\alpha}_{\lambda_V\lambda'_V}(1+\epsilon R)^{-1}, & \alpha = 1,2,3, \\ \sqrt{R}\rho^{\alpha}_{\lambda_V\lambda'_V}(1+\epsilon R)^{-1}, & \alpha = 5,6,7,8. \end{cases} \tag{5}$$

The quantity $R = d\sigma_L/d\sigma_T$ is the longitudinal-to-transverse cross-section ratio of virtual photons and ϵ the virtual-photon polarisation parameter given in Eq. (20). There are in total 23 SDMEs defined in Eq. (5). The relations between these SDMEs and the corresponding helicity amplitudes are provided in Appendix A of Ref. [22].

2.2 Properties of Helicity Amplitudes

Each helicity amplitude $F \equiv F_{\lambda_V\lambda'_N\lambda_\gamma\lambda_N}$ can be decomposed linearly into a natural-parity-exchange (NPE) amplitude T and an unnatural-parity-exchange (UPE) amplitude U [1, 22]: $F = T + U$. The NPE and UPE amplitudes are related to helicity amplitudes as follows [1]:

$$T_{\lambda_V\lambda'_N\lambda_\gamma\lambda_N} = \frac{1}{2}[F_{\lambda_V\lambda'_N\lambda_\gamma\lambda_N} + (-1)^{\lambda_V-\lambda_\gamma}F_{-\lambda_V\lambda'_N-\lambda_\gamma\lambda_N}], \tag{6}$$

$$U_{\lambda_V\lambda'_N\lambda_\gamma\lambda_N} = \frac{1}{2}[F_{\lambda_V\lambda'_N\lambda_\gamma\lambda_N} - (-1)^{\lambda_V-\lambda_\gamma}F_{-\lambda_V\lambda'_N-\lambda_\gamma\lambda_N}]. \tag{7}$$

The asymptotic behaviour of amplitudes F at small t' was derived from angular-momentum conservation [30] and reads [2]

$$F_{\lambda_V\lambda'_N\lambda_\gamma\lambda_N} \propto \left(\frac{\sqrt{t'}}{M}\right)^{|(\lambda_V-\lambda'_N)-(\lambda_\gamma-\lambda_N)|}. \tag{8}$$

Here and in the following M denotes the proton mass. Equations (6-8) show that double-helicity-flip amplitudes with $|\lambda_V - \lambda_\gamma| = 2$ are suppressed at least by a factor of $\sqrt{t'}/M$, and that their contributions to SDMEs are suppressed by t'/M^2.

Introducing the notation

$$\widetilde{\sum} T_{\lambda_V\lambda_\gamma}T^*_{\lambda'_V\lambda'_\gamma} \equiv \frac{1}{2}\sum_{\lambda_N\lambda'_N} T_{\lambda_V\lambda'_N\lambda_\gamma\lambda_N}T^*_{\lambda'_V\lambda'_N\lambda'_\gamma\lambda_N} \tag{9}$$

and the symmetry properties [1, 22] of the amplitudes T, Eq. (9) becomes

$$\widetilde{\sum} T_{\lambda_V \lambda_\gamma} T^*_{\lambda'_V \lambda'_\gamma} = T_{\lambda_V \frac{1}{2} \lambda_\gamma \frac{1}{2}} T^*_{\lambda'_V \frac{1}{2} \lambda'_\gamma \frac{1}{2}} + T_{\lambda_V -\frac{1}{2} \lambda_\gamma \frac{1}{2}} T^*_{\lambda'_V -\frac{1}{2} \lambda'_\gamma \frac{1}{2}}. \tag{10}$$

Note that the first product TT^* on the right-hand side represents contributions from NPE amplitudes without nucleon-helicity flip, while the second product of NPE amplitudes TT^* includes a nucleon-helicity flip. The relations for the UPE amplitudes can be written in an analogous way. For brevity, the nucleon-helicity indices will be omitted for amplitudes with $\lambda_N = \lambda'_N$ in the following, i.e.,

$$\begin{aligned} T_{\lambda_V \lambda_\gamma} &\equiv T_{\lambda_V \frac{1}{2} \lambda_\gamma \frac{1}{2}} &&= T_{\lambda_V -\frac{1}{2} \lambda_\gamma -\frac{1}{2}}, \\ U_{\lambda_V \lambda_\gamma} &\equiv U_{\lambda_V \frac{1}{2} \lambda_\gamma \frac{1}{2}} &&= -U_{\lambda_V -\frac{1}{2} \lambda_\gamma -\frac{1}{2}}. \end{aligned} \tag{11}$$

The assumption that there exist only diagonal $\gamma^* \to V$ transitions ($\lambda_V = \lambda_\gamma$) is usually referred to as hypothesis of s-channel helicity conservation.

3 Experimental access to SDMEs

Spin density matrix elements are extracted from COMPASS data in exclusive muoproduction of ρ^0 mesons (Eq. (1)). The SDMEs are fitted as parameters of the three-dimensional angular distribution $W^{U+L}(\Phi, \phi, \cos\Theta)$ to the corresponding experimental distribution. The angles and reference frames for the production and decay process $\mu N \to \mu N' \rho^0$ ($\rho^0 \to \pi^+\pi^-$) are shown in Fig. 1.

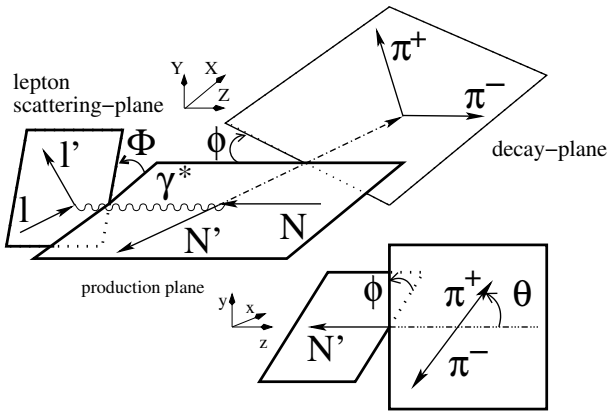

Fig. 1: Definition of angles in the process $\mu N \to \mu' N' \rho^0$ with $\rho^0 \to \pi^+\pi^-$. Here, Φ is the angle between the ρ^0 production plane and the lepton scattering plane in the centre-of-mass system of the virtual photon and the target nucleon, while ϕ is the angle between the ρ^0 production and decay planes. The variable Θ is the polar angle of the decay π^+ in the ρ^0 meson rest frame.

The right-handed "hadronic CM system" of virtual photon and target nucleon is identical to that used in Ref. [31].

The directions of axes of the hadronic CM system and the ρ^0-meson rest frame coincide with the directions of axes of the helicity frame [1, 22, 33]. The angles Φ, ϕ, and Θ involved in ρ^0-meson production and decay are defined as follows [22]. The azimuthal angle Φ between ρ^0-meson production plane and lepton scattering plane in the hadronic CM system is given by:

$$\cos\Phi = \frac{(\mathbf{q}\times\mathbf{v})\cdot(\mathbf{k}\times\mathbf{k}')}{|\mathbf{q}\times\mathbf{v}|\cdot|\mathbf{k}\times\mathbf{k}'|}, \tag{12}$$

$$\sin\Phi = \frac{[(\mathbf{q}\times\mathbf{v})\times(\mathbf{k}\times\mathbf{k}')]\cdot\mathbf{q}}{|\mathbf{q}\times\mathbf{v}|\cdot|\mathbf{k}\times\mathbf{k}'|\cdot|\mathbf{q}|}. \tag{13}$$

Here, $\mathbf{k}$, $\mathbf{k}'$, $\mathbf{q} = \mathbf{k} - \mathbf{k}'$, and $\mathbf{v}$ are the three-momenta of the incoming and outgoing lepton, the virtual photon, and the ρ^0 meson respectively. The azimuthal angle ϕ between ρ^0-meson decay and production planes is defined by:

$$\cos\phi = \frac{(\mathbf{q}\times\mathbf{v})\cdot(\mathbf{v}\times\mathbf{p}_{\pi^+})}{|(\mathbf{q}\times\mathbf{v})|\cdot|\mathbf{v}\times\mathbf{p}_{\pi^+}|}, \tag{14}$$

$$\sin\phi = \frac{[(\mathbf{q}\times\mathbf{v})\times\mathbf{v}]\cdot(\mathbf{p}_{\pi^+}\times\mathbf{v})}{|(\mathbf{q}\times\mathbf{v})\times\mathbf{v}|\cdot|\mathbf{p}_{\pi^+}\times\mathbf{v}|}, \tag{15}$$

where $\mathbf{p}_{\pi^+}$ is the three-momentum of the positively charged decay pion π^+ in the hadronic CM system. The polar angle Θ of the decay π^+ in the vector-meson rest frame, with the z-axis aligned opposite to the outgoing nucleon three-momentum $\mathbf{P}'$ and the y-axis directed along $\mathbf{P}'\times\mathbf{q}$, is given by:

$$\cos\Theta = -\frac{\mathbf{P}'\cdot\mathbf{P}_{\pi^+}}{|\mathbf{P}'|\cdot|\mathbf{P}_{\pi^+}|}, \tag{16}$$

where $\mathbf{P}_{\pi^+}$ is the three-momentum of the positively charged decay pion in the vector-meson rest frame.

The angular distribution $\mathcal{W}^{U+L}$ is decomposed into contributions that are not coupled ($\mathcal{W}^U$ - unpolarised) or coupled ($\mathcal{W}^L$ - polarised) to the longitudinal beam polarisation P_b:

$$\mathcal{W}^{U+L}(\Phi,\phi,\cos\Theta) = \mathcal{W}^U(\Phi,\phi,\cos\Theta) + P_\mathrm{b}\mathcal{W}^L(\Phi,\phi,\cos\Theta). \tag{17}$$

Since the data were collected with longitudinally polarised muon beams, both unpolarised and polarised SDMEs can be accessed, allowing the extraction of 15 unpolarised SDMEs from $\mathcal{W}^U$:

$$\begin{aligned}
\mathcal{W}^U(\Phi,\phi,\cos\Theta) &= \frac{3}{8\pi^2}\Bigg[\frac{1}{2}(1-r^{04}_{00}) + \frac{1}{2}(3r^{04}_{00}-1)\cos^2\Theta \\
&- \sqrt{2}\mathrm{Re}\{r^{04}_{10}\}\sin 2\Theta\cos\phi - r^{04}_{1-1}\sin^2\Theta\cos 2\phi \\
&- \epsilon\cos 2\Phi\Big(r^1_{11}\sin^2\Theta + r^1_{00}\cos^2\Theta - \sqrt{2}\mathrm{Re}\{r^1_{10}\}\sin 2\Theta\cos\phi - r^1_{1-1}\sin^2\Theta\cos 2\phi\Big) \\
&- \epsilon\sin 2\Phi\Big(\sqrt{2}\mathrm{Im}\{r^2_{10}\}\sin 2\Theta\sin\phi + \mathrm{Im}\{r^2_{1-1}\}\sin^2\Theta\sin 2\phi\Big) \\
&+ \sqrt{2\epsilon(1+\epsilon)}\cos\Phi\Big(r^5_{11}\sin^2\Theta + r^5_{00}\cos^2\Theta - \sqrt{2}\mathrm{Re}\{r^5_{10}\}\sin 2\Theta\cos\phi \\
&- r^5_{1-1}\sin^2\Theta\cos 2\phi\Big) \\
&+ \sqrt{2\epsilon(1+\epsilon)}\sin\Phi\Big(\sqrt{2}\mathrm{Im}\{r^6_{10}\}\sin 2\Theta\sin\phi + \mathrm{Im}\{r^6_{1-1}\}\sin^2\Theta\sin 2\phi\Big)\Bigg],
\end{aligned} \tag{18}$$

and the extraction of 8 polarised SDMEs from $\mathcal{W}^L$:

$$\begin{aligned}
\mathcal{W}^L(\Phi,\phi,\cos\Theta) &= \frac{3}{8\pi^2}\Bigg[\sqrt{1-\epsilon^2}\Big(\sqrt{2}\mathrm{Im}\{r^3_{10}\}\sin 2\Theta\sin\phi + \mathrm{Im}\{r^3_{1-1}\}\sin^2\Theta\sin 2\phi\Big) \\
&+ \sqrt{2\epsilon(1-\epsilon)}\cos\Phi\Big(\sqrt{2}\mathrm{Im}\{r^7_{10}\}\sin 2\Theta\sin\phi + \mathrm{Im}\{r^7_{1-1}\}\sin^2\Theta\sin 2\phi\Big) \\
&+ \sqrt{2\epsilon(1-\epsilon)}\sin\Phi\Big(r^8_{11}\sin^2\Theta + r^8_{00}\cos^2\Theta - \sqrt{2}\mathrm{Re}\{r^8_{10}\}\sin 2\Theta\cos\phi \\
&- r^8_{1-1}\sin^2\Theta\cos 2\phi\Big)\Bigg].
\end{aligned} \tag{19}$$

The virtual-photon polarisation parameter ϵ, which represents the ratio of fluxes of longitudinal and transverse virtual photons, is given by:

$$\epsilon = \frac{1 - y - y^2 \frac{Q^2}{4\nu^2}}{1 - y + \frac{1}{4} y^2 (\frac{Q^2}{\nu^2} + 2)}, \tag{20}$$

where $y = p \cdot q / p \cdot k \overset{\text{lab}}{=} \nu / E$. The symbols p, q and k denote the four-momenta of target proton, virtual photon and incident lepton respectively. The energy of virtual photon and incident lepton in the target rest frame is denoted by ν and E, respectively.

4 Experimental setup and data selection

The fixed-target experiment COMPASS is located at CERN in the M2-beamline of the Super Proton Synchrotron (SPS). The experiment consists of a versatile setup that can use variety of targets, detectors and make use of different beams. It uses a two-stage spectrometer with a number of tracking and particle identification detectors placed over a length of approximately 60 m. Each stage of the spectrometer is built around one of the two dipole magnets (SM1 and SM2). The first stage covers large scattering angles up to 180 mrad, and the second stage smaller scattering angles down to 0.5 mrad. More detailed descriptions of the COMPASS experiment can be found in Refs. [35–37].

In this paper, we analyse data collected during 4 weeks in 2012 that were dedicated to the pilot run of a program designed to study GPDs and hadron tomography through Deeply Virtual Compton Scattering (DVCS) and HEMP processes. The experiment made use of the 160 GeV/c polarised muon beam and an unpolarised liquid-hydrogen target. The target was surrounded by a time-of-flight (TOF) system for the detection of recoil protons. The use of the recoil-proton detector (RPD) is important in the studies of the DVCS process, but for HEMP processes, like ρ^0-meson production, it restricts the kinematic coverage, so that the RPD information is not used in the present analysis.

The muon beam originates from in-flight decays of pions and kaons produced by SPS protons impinging on a primary target. Due to the weak nature of the decay, the muon beam is naturally polarised. The beam is negatively polarised for μ^+ and positively polarised for μ^-, and the achieved absolute value of polarisation is $(80 \pm 4)\%$. The data has been taken using both μ^+ and μ^- beams. The SM1 and SM2 spectrometer magnets polarities were changed accordingly with beam charge to ensure equal acceptance of the COMPASS spectrometer in both cases.

The analysis is focused on the process

$$\begin{aligned} \mu p &\to \mu' p' \rho^0 \\ &\hookrightarrow \quad \pi^+\pi^- \qquad\qquad \text{BR} \approx 99\%, \end{aligned}$$

which defines the topology of the accepted events. The events are required to have two hadron tracks of opposite charge and one reconstructed vertex inside the target with incoming and outgoing muon associated. The outgoing muon is required to traverse more than 15 radiation lengths of material and to have the same charge as the incoming muon. Charged hadron tracks are identified by requiring to traverse less than 10 radiation lengths of material.

4.1 Kinematic selections

In order to select exclusively produced ρ^0 mesons, events are required to meet the following kinematic constraints:

- $1.0\ (\mathrm{GeV}/c)^2 < Q^2 < 10.0\ (\mathrm{GeV}/c)^2$, which selects the region of perturbative QCD (lower limit) and suppresses background from hadrons produced in DIS, hereafter referred to as "SIDIS background" (upper limit);
- $0.1 < y < 0.9$ to remove events that are poorly reconstructed (lower limit) and events with large radiative corrections (upper limit);
- $W > 5.0\ \mathrm{GeV}/c^2$ to avoid significant fluctuations in the cross section that appear in the lower W region because of the production of resonances;
- $\nu > 20$ GeV, which is the energy of the virtual photon (in the laboratory system);
- $0.01\ (\mathrm{GeV}/c)^2 < p_T^2 < 0.5\ (\mathrm{GeV}/c)^2$ to remove events with poorly determined azimuthal angle (lower limit) and to suppress SIDIS background (upper limit);
- $P_{\rho^0} > 15\ \mathrm{GeV}/c$ to reduce the SIDIS background contribution, where P_{ρ^0} is the ρ^0 momentum;
- $0.5\ \mathrm{GeV}/c^2 < M_{\pi^+\pi^-} < 1.1\ \mathrm{GeV}/c^2$ to select ρ^0 mesons, where $M_{\pi^+\pi^-}$ is the two-pion invariant mass.

In order to select exclusively produced ρ^0 mesons, the missing energy

$$E_{\mathrm{miss}} = \frac{M_X^2 - M^2}{2M} \tag{21}$$

is used. Here $M_X^2 = (p + q - p_{\pi^+} - p_{\pi^-})^2$ is the missing mass squared, $p_{\pi^+(\pi^-)}$ the pion four-momenta and M the mass of the proton. In order to account for experimental resolution the selection -2.5 GeV $< E_{\mathrm{miss}} < 2.5$ GeV is applied. The distribution of the missing energy is shown in Fig. 3, where the exclusive peak in the experimental data appears within the selection limits.

After having applied all the selection requirements, the data set for physics analysis consists of 23785 events taken with the μ^+ beam and 28472 events with the μ^- beam.

4.2 Invariant mass distribution

The two-pion invariant mass distribution is shown in Fig. 2. A clear ρ^0 signal is observed. Background coming from exclusive production of ϕ and its decay $\phi \to K^+K^-$, where the kaons are misidentified as pions, is expected and seen at $M_{\pi^+\pi^-} < 0.4\ \mathrm{GeV}/c^2$. Therefore, applying the selection $0.5\ \mathrm{GeV}/c^2 < M_{\pi^+\pi^-} < 1.1\ \mathrm{GeV}/c^2$ removes this background. The distribution for the experimental data is compared to that for the reconstructed events of Monte Carlo (MC) events obtained with the HEPGEN++ ρ^0 generator, in the following denoted by HEPGEN [41, 42]. As in HEPGEN only exclusive ρ^0 production is generated, while the data contains both exclusive resonant and non-resonant $\pi^+\pi^-$ production as well as their interference, a difference in shapes between the experimental and simulated distributions is observed. The effect is in agreement with the expectation from the Söding model [44], which predicts a sizeable interference between the small amplitude for non-resonant $\pi^+\pi^-$ pair production and the large one for resonant $\pi^+\pi^-$ production. The characteristic prediction of the model is the change of the sign of the interference term at the maximum of the ρ^0 resonance from being positive at smaller values of $M_{\pi^+\pi^-}$ to negative at larger $M_{\pi^+\pi^-}$ values.

In order to evaluate the contribution of non-resonant $\pi^+\pi^-$ pair production, the following procedure is used. The invariant mass distribution from HEPGEN is normalised to the data in the region $0.75\ \mathrm{GeV}/c^2 < M_{\pi^+\pi^-} < 0.77\ \mathrm{GeV}/c^2$. The difference between the integrals of the distributions for the data and HEPGEN over the full range $0.5\ \mathrm{GeV}/c^2 < M_{\pi^+\pi^-} < 1.1\ \mathrm{GeV}/c^2$ is approximately equal to the global contribution of non-resonant production. This contribution, which includes the interference between the

amplitudes for resonant and non-resonant production as well as the squared amplitude for the latter one, is equal to about 3% and hence neglected.

In addition, the $\omega \to \pi^+\pi^-$ channel, with a branching fraction of 1.5%, gives an irreducible background to the ρ^0 channel. As the branching fraction is small and the contribution of $\rho^0 - \omega$ interference was found to be very small [20], the contribution of $\omega \to \pi^+\pi^-$ channel is neglected in this analysis.

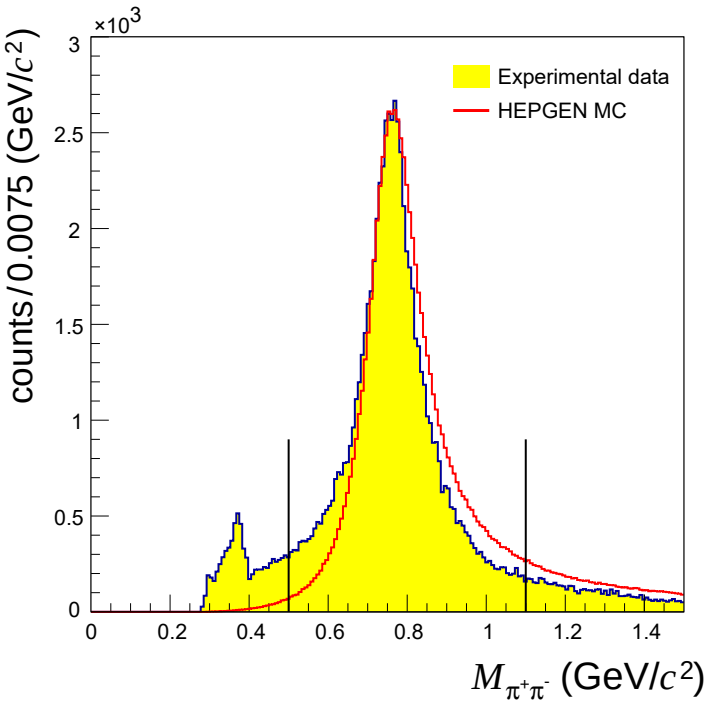

Fig. 2: Distribution of the $\pi^+\pi^-$ invariant mass for experimental data (shaded histogram) and HEPGEN MC (open histogram). The invariant mass distribution from HEPGEN is normalised to the data in the region 0.75 GeV/c^2 < $M_{\pi^+\pi^-}$ < 0.77 GeV/c^2. The vertical lines indicate the applied limits.

4.3 Backgrounds for exclusive ρ^0 production

i) *SIDIS background*

The largest background contribution is due to the SIDIS background, i.e., events with hadrons produced in DIS. In order to determine the fraction of SIDIS background in the selected ρ^0 events, the E_{miss} distribution is used as shown in Fig. 3. The procedure is described in detail in Refs. [34, 38]. The SIDIS background simulation is performed using the LEPTO 6.5.1 generator with the COMPASS tuning of parameters [39] and processed with the simulation of the COMPASS setup [40]. The LEPTO simulated background is shown in Fig. 3 as the blue points. The simulated events are selected using the same criteria as for the experimental data. In order to improve the agreement between LEPTO events and the data, the simulated events are reweighted. For this purpose, events with the same-sign hadron pairs are selected. The reweighting is applied on a bin-by-bin basis to the E_{miss} distribution with the following weight:

$$w(E_{\text{miss}}) = \frac{N_{\text{D}}^{\text{sc}}(E_{\text{miss}})}{N_{\text{MC}}^{\text{sc}}(E_{\text{miss}})}. \tag{22}$$

Here $N_{\text{D}}^{\text{sc}}(E_{\text{miss}})$ ($N_{\text{MC}}^{\text{sc}}(E_{\text{miss}})$) is the number of events with same-sign hadron pairs selected from experimental (D) or simulated (MC) data.

The distribution of the LEPTO simulated events is normalised to the experimental data in the background dominated region of 7 GeV $< E_{\text{miss}} <$ 20 GeV. The procedure estimates the background fraction f_{bg} for the selected ρ^0 to be 0.17 in the signal region -2.5 GeV $< E_{\text{miss}} <$ 2.5 GeV. However, it was found that the fraction of SIDIS background changes within the kinematic coverage of this measurement, in particular it is increasing with increasing Q^2 and p_{T}^2 and with decreasing W. Therefore, the background fraction is estimated in each kinematic bin separately, resulting in values of f_{bg} from 0.10 to 0.32 for the determination of the SDME values as functions of kinematic variables.

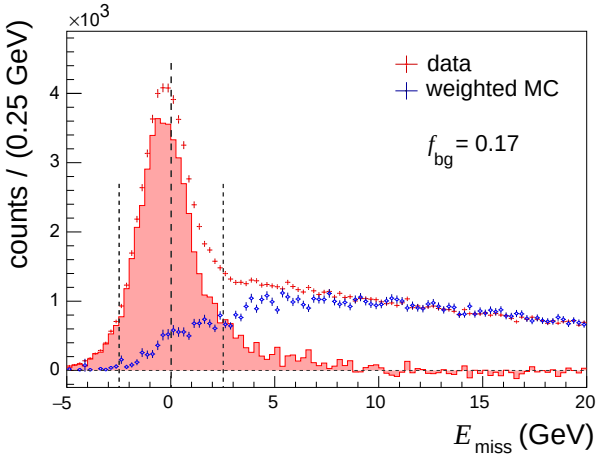

Fig. 3: The missing-energy distribution from experimental data (red points) compared to the distribution of SIDIS events from a LEPTO MC simulation (blue points). The MC distribution is normalised to the data in the region 7 GeV $< E_{\text{miss}} <$ 20 GeV. The background-corrected distribution for the data is shown as shaded histogram. The vertical lines at $|E_{\text{miss}}| = 2.5$ GeV indicate the limits of the exclusive region. Each LEPTO MC event is reweighted by a E_{miss}-dependent weight that is calculated using both experimental and simulated data with same-charge hadron pairs. See text for a detailed explanation.

ii) *Background from proton-dissociation processes*

This background is due to the processes $\gamma^* + p \to \rho^0 + N^*$ with a baryon N^* decaying into a system of hadrons. As observed by HERA experiments, the cross section for such process, when integrated over all N^* states, is at the level of 20% of the cross section for exclusive ρ^0 production [29]. In the present analysis such processes are suppressed by the applied selections, in particular on E_{miss} and p_{T}^2, which reduce the contribution from proton-dissociation by a factor of 2. As it is reported in Refs. [26, 28] that the angular distributions for ρ^0 decay and production in the exclusive and proton-dissociation channels are compatible, no correction is applied for proton-dissociation events.

iii) *Other backgrounds*

In addition to the background contributions discussed above and in Sec. 4.2, several others were considered in Ref. [26]. They may originate from the processes $\omega \to \pi^+\pi^-\pi^0$, $\phi \to \rho\pi$, $\phi \to \pi^+\pi^-\pi^0$ and $\rho' \to \pi^+\pi^-\pi^0\pi^0$. These events are expected to be strongly suppressed after applying the selections on E_{miss} and p_{T}^2 and their contributions are neglected in the present analysis.

5 Extraction of SDMEs

5.1 Unbinned Maximum Likelihood method

The method to determine SDMEs was described in Sec. 3. Equations (17, 18, 19) relate the angular distribution $\mathcal{W}$ to the 23 SDMEs $r^{\alpha}_{\lambda_V \lambda'_V}$. In order to extract SDME values in this measurement, the Unbinned Maximum Likelihood (UML) method is used to fit the experimental three-dimensional angular

distribution of ρ^0 production and decay to the function $\mathcal{W}(\mathcal{R};\Phi,\phi,\cos\Theta)$, where $\mathcal{R}$ is the set of the 23 SDMEs. In the fit, the negative log-likelihood function

$$-\ln L(\mathcal{R}) = -\sum_{i=1}^{N} \ln \frac{\mathcal{W}^{U+L}(\mathcal{R};\Phi_i,\phi_i,\cos\Theta_i)}{\widetilde{\mathcal{N}}(\mathcal{R})} \tag{23}$$

is minimised. Here, N represents the number of selected events and $\mathcal{N}(\mathcal{R})$ is the likelihood normalisation factor defined as

$$\widetilde{\mathcal{N}}(\mathcal{R}) = \sum_{j=1}^{N_{\mathrm{MC}}} \mathcal{W}^{U+L}(\mathcal{R};\Phi_j,\phi_j,\cos\Theta_j), \tag{24}$$

where N_{MC} is the number of simulated ρ^0 events generated by the HEPGEN generator [41, 42]. In order to simulate exclusive ρ^0 production, the option of an isotropic three-dimensional angular distribution of ρ^0 production and decay was chosen. The generated events are further processed with the simulation of the COMPASS setup [40]. Identical selection requirements are applied as for the experimental data.

5.2 Background-corrected SDMEs

The above described procedure of SDME extraction does not account for the SIDIS background contamination. In order to determine the background-corrected SDMEs, a two-step approach is applied.

In the first step, the 23 "background SDMEs" are determined using a parameterisation of the background angular distributions. The SIDIS background events simulated by the LEPTO generator are treated by the same method as described above. The UML fit is performed in the signal region, $-2.5\ \mathrm{GeV} < E_{\mathrm{miss}} < 2.5\ \mathrm{GeV}$ according to Eq. (23), resulting in the set $\mathcal{R}_{\mathrm{bg}}$ of background SDMEs.

In the second step, the set $\mathcal{R}_{\mathrm{bg}}$ and the background fraction f_{bg} determined in Sec. 4.3 are used to extract the set $\mathcal{R}_{\mathrm{sig}}$ of the background-corrected SDMEs by fitting the negative log-likelihood function

$$-\ln L(\mathcal{R}_{\mathrm{sig}}) = -\sum_{i=1}^{N} \ln\Big[\frac{(1-f_{\mathrm{bg}})\,\mathcal{W}^{U+L}(\mathcal{R}_{\mathrm{sig}};\Phi_i,\phi_i,\cos\Theta_i)}{\widetilde{\mathcal{N}}(\mathcal{R}_{\mathrm{sig}},\mathcal{R}_{\mathrm{bg}})} + \frac{f_{\mathrm{bg}}\,\mathcal{W}^{U+L}(\mathcal{R}_{\mathrm{bg}};\Phi_i,\phi_i,\cos\Theta_i)}{\widetilde{\mathcal{N}}(\mathcal{R}_{\mathrm{sig}},\mathcal{R}_{\mathrm{bg}})}\Big]. \tag{25}$$

Here, $\widetilde{\mathcal{N}}$ is the likelihood normalisation factor defined as

$$\widetilde{\mathcal{N}}(\mathcal{R}_{\mathrm{sig}},\mathcal{R}_{\mathrm{bg}}) = \sum_{j=1}^{N_{MC}} \left[(1-f_{\mathrm{bg}})\,\mathcal{W}^{U+L}(\mathcal{R}_{\mathrm{sig}};\Phi_j,\phi_j,\cos\Theta_j) + f_{\mathrm{bg}}\,\mathcal{W}^{U+L}(\mathcal{R}_{\mathrm{bg}};\Phi_j,\phi_j,\cos\Theta_j)\right]. \tag{26}$$

5.3 Systematic uncertainties

The systematic uncertainties of the measured SDME values are considered to arise from the following sources:

i) *Difference between μ^+ and μ^- beam*
In the measurement, μ^+ and μ^- beams were used, which were not identical in terms of intensity. The intensity of the μ^+ beam was higher by a factor of approximately 2.7 than that of the μ^- beam. In order to account for a possible impact of this difference on the measured SDMEs, the latter are extracted separately for μ^+ and μ^- data, and half of the difference between the two results is assigned as systematic uncertainty.

ii) *Position of the E_{miss} peak*
As observed in Fig. 3, the signal peak in the E_{miss} distribution is not centred at zero, but rather slightly shifted towards negative values. The reason for this shift is a small imbalance between

the measured incoming muon energy and energies of the measured final state particles in the spectrometer. Some SDME values depend on the position of this peak [43], hence a systematic uncertainty is assigned based on the difference between the SDMEs extracted without and with a correction of +0.25 GeV/c to the beam momentum to centre the E_{miss} peak at zero. It was checked that this method of the beam momentum correction yields a similar systematic uncertainty as in case of the method that rescales the measured momenta of the final-state particles to centre the E_{miss} peak position at zero.

iii) *Dependence on the background angular distribution*
The method to evaluate the background-corrected SDMEs, described in Sec. 5.2, uses the LEPTO generated events for the estimation of the SIDIS background SDMEs in the signal region -2.5 GeV $< E_{\text{miss}} < 2.5$ GeV. Note that the LEPTO generator was not tuned to reproduce the experimental angular distributions in the specific phase space of this analysis. In order to account for a possible source of uncertainty, another procedure was applied to estimate the background SDMEs using the background-dominated region 7.0 GeV$< E_{\text{miss}} <$ 20.0 GeV in the experimental data. The systematic uncertainty is assigned based on the difference between the two methods of evaluating the background SDMEs.

iv) *Uncertainty in the determination of the background fraction*
Another contribution to the systematic uncertainty of SDME values is related to the uncertainty of the background fraction determination. It is estimated to be about 1% based on the comparison of background fraction values that were evaluated using two different methods to normalise LEPTO MC results with respect to experimental data. The difference between the respective SDME values is taken as systematic uncertainty.

v) *Sensitivity to the shapes of the kinematic distributions generated by HEPGEN*
The SDME values can be sensitive to the shapes of the kinematic distributions generated by the HEPGEN generator. In order to check for such an effect, the SDMEs were extracted using modified HEPGEN weights so that the reconstructed MC Q^2 and ν distributions match those of the experimental data. Although the effect on the measured SDMEs is fairly small, the difference between the extraction using the original simulated sample and the one with reweighting is assigned as systematic uncertainty.

The contributions from the described sources of systematic uncertainties are shown individually in the Appendix in Table A.1. The largest source is typically from group i) (the difference between the μ^+ and μ^- beams), followed by group ii) (shift in the E_{miss} peak position) and group iii) (dependence on the background angular distribution). The systematic uncertainties arising from the above discussed sources are added in quadrature to obtain the total systematic uncertainty. The 23 SDMEs measured over the entire COMPASS kinematic region are given in Table 1 together with their statistical and total systematic uncertainties. For most SDMEs the total systematic uncertainty is larger than the statistical uncertainty.

6 Results

6.1 SDMEs for the entire kinematic region

The kinematic region is defined as: 1.0 (GeV/c)^2 $< Q^2 <$ 10.0 (GeV/c)^2, 5.0 GeV/c^2 $< W <$ 17.0 GeV/c^2 and 0.01 (GeV/c)^2 $< p_{\text{T}}^2 <$ 0.5 (GeV/c)^2, with mean values $\langle Q^2 \rangle$ = 2.40 (GeV/c)^2, $\langle W \rangle$ = 9.9 GeV/c^2 and $\langle p_{\text{T}}^2 \rangle$ = 0.18 (GeV/c)^2. The SDMEs extracted in this region are presented in Fig. 4 and Table 1. Following Refs. [22, 31] they are assembled in five classes corresponding to different helicity transitions. In Fig. 4, polarised SDMEs are shown in shaded areas.

The dominant contributions to the SDMEs in class A are related to the squared amplitudes for transitions from longitudinally polarised virtual photons to longitudinally polarised vector mesons, $\gamma^*_L \to V_L$, and from transversely polarised virtual photons to transversely polarised vector mesons, $\gamma^*_T \to V_T$. The former ones appear in the SDME r^{04}_{00}, and the latter ones in the SDMEs r^1_{1-1} and Im r^2_{1-1}, which approximately mirror each other value (see Fig. 4 and Table 1). The dominant terms in class B correspond to the interference between amplitudes for the two aforementioned transitions. The SDMEs of this class allow the determination of the phase difference between the amplitude T_{11} for $\gamma^*_T \to V_T$ transitions and the amplitude T_{00} for $\gamma^*_L \to V_L$ transition (*cf* Sec. 7.6). In class C, the main terms in most of the SDMEs are proportional to the interference between the helicity-flip amplitude T_{01}, describing $\gamma^*_T \to V_L$ transitions, and the large helicity-conserving amplitudes, either T_{11} (for Re r^{04}_{10}, Re r^1_{10}, Im r^2_{10}, Im r^3_{10}) or T_{00} (for r^5_{00}, r^8_{00}). The dominant terms in the SDMEs of classes D and E are proportional to the interference between the amplitude T_{11} and small amplitudes describing $\gamma^*_L \to V_T$ and $\gamma^*_T \to V_{-T}$ transitions, respectively.

The experimental uncertainties of the polarised SDMEs are in most of the cases larger than those of the unpolarised ones because the lepton-beam polarisation is smaller than unity ($|P_b| \approx 80\%$), and in the expressions for the angular distributions (see Eq. (19)) they are multiplied by the small factor $|P_b|\sqrt{1-\epsilon}$, where $\epsilon \approx 0.90$.

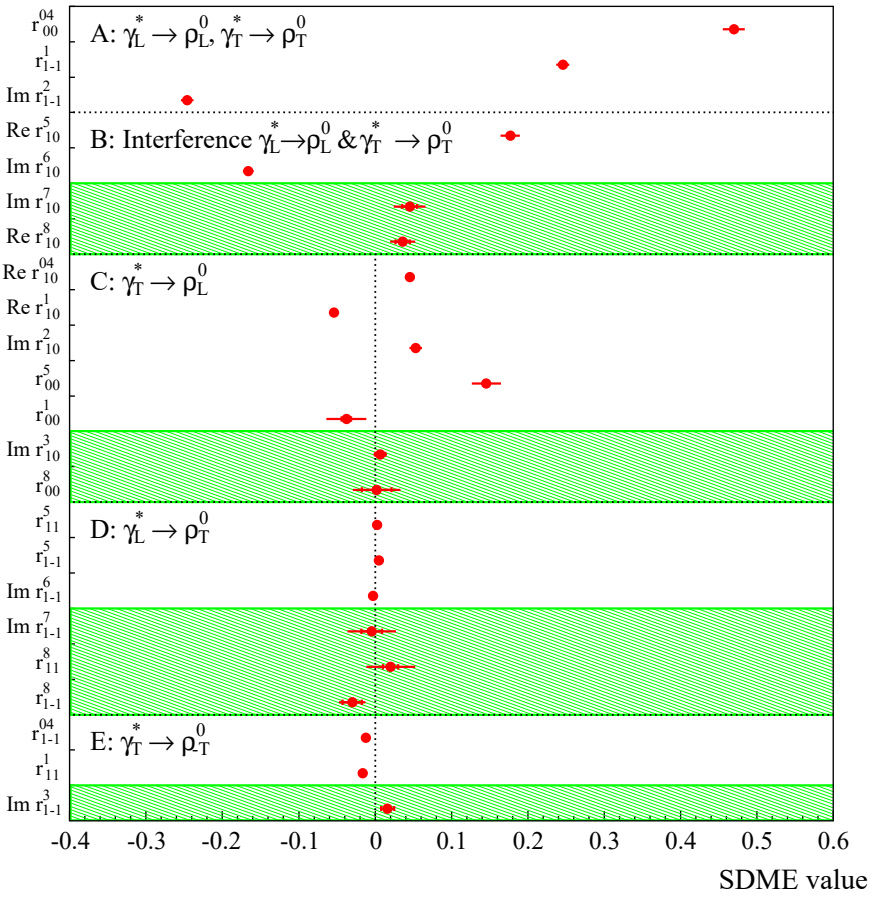

Fig. 4: The 23 SDMEs for exclusive ρ^0 leptoproduction extracted in the entire COMPASS kinematic region with $\langle Q^2 \rangle = 2.40$ (GeV/c)^2, $\langle W \rangle = 9.9$ GeV/c^2, $\langle p_T^2 \rangle = 0.18$ (GeV/c)^2. Inner error bars represent statistical uncertainties and outer ones statistical and systematic uncertainties added in quadrature. Unpolarised (polarised) SDMEs are displayed in unshaded (shaded) areas.

Table 1: The 23 unpolarised and polarised SDMEs for the entire COMPASS kinematic region, shown in the same order as in Fig. 4 for classes A to E. The first uncertainties are statistical, the second systematic.

SDME	
r^{04}_{00}	$0.4698 \pm 0.0035 \pm 0.0220$
r^{1}_{1-1}	$0.2457 \pm 0.0037 \pm 0.0064$
Im r^{2}_{1-1}	$-0.2459 \pm 0.0038 \pm 0.0049$
Re r^{5}_{10}	$0.1769 \pm 0.0015 \pm 0.0041$
Im r^{6}_{10}	$-0.1662 \pm 0.0014 \pm 0.0040$
Im r^{7}_{10}	$0.0453 \pm 0.0096 \pm 0.0156$
Re r^{8}_{10}	$0.0362 \pm 0.0095 \pm 0.0121$
Re r^{04}_{10}	$0.0454 \pm 0.0021 \pm 0.0058$
Re r^{1}_{10}	$-0.0539 \pm 0.0029 \pm 0.0040$
Im r^{2}_{10}	$0.0532 \pm 0.0028 \pm 0.0043$
r^{5}_{00}	$0.1456 \pm 0.0033 \pm 0.0129$
r^{1}_{00}	$-0.0376 \pm 0.0062 \pm 0.0114$
Im r^{3}_{10}	$0.0067 \pm 0.0067 \pm 0.0045$
r^{8}_{00}	$0.0019 \pm 0.0194 \pm 0.0253$
r^{5}_{11}	$0.0027 \pm 0.0016 \pm 0.0025$
r^{5}_{1-1}	$0.0050 \pm 0.0020 \pm 0.0025$
Im r^{6}_{1-1}	$-0.0028 \pm 0.0020 \pm 0.0019$
Im r^{7}_{1-1}	$-0.0045 \pm 0.0134 \pm 0.0224$
r^{8}_{11}	$0.0203 \pm 0.0101 \pm 0.0305$
r^{8}_{1-1}	$-0.0300 \pm 0.0128 \pm 0.0091$
r^{04}_{1-1}	$-0.0120 \pm 0.0027 \pm 0.0032$
r^{1}_{11}	$-0.0162 \pm 0.0032 \pm 0.0037$
Im r^{3}_{1-1}	$0.0163 \pm 0.0085 \pm 0.0043$

6.2 Dependences of SDMEs on Q^2, p_T^2 and W

The SDMEs values extracted in four kinematic bins of Q^2, p_T^2, or W are shown in Figs. 5, 6 and 7. The limits of the kinematic bins and the mean values of kinematic variables in each bin are given in Table 2.

The value of the SDME r^{04}_{00}, which corresponds to the fractional contribution of $|T_{00}|^2$ from longitudinally polarised virtual photons to the cross section, increases with Q^2 and p_T^2, while the opposite trend is observed for the absolute values of the SDMEs r^{1}_{1-1} and Im r^{2}_{1-1}, which represent the fractional contribution of $|T_{11}|^2$ from transversely polarised virtual photons. In class C a sizeable increase of r^{5}_{00} with Q^2 is observed. As a consequence of angular-momentum conservation the helicity single and double-flip amplitudes should vanish as $p_T^2 \to 0$, which is consistent with the measured p_T^2-dependence of SDMEs in classes C, D and E. No clear W-dependence is observed for any of 23 SDMEs.

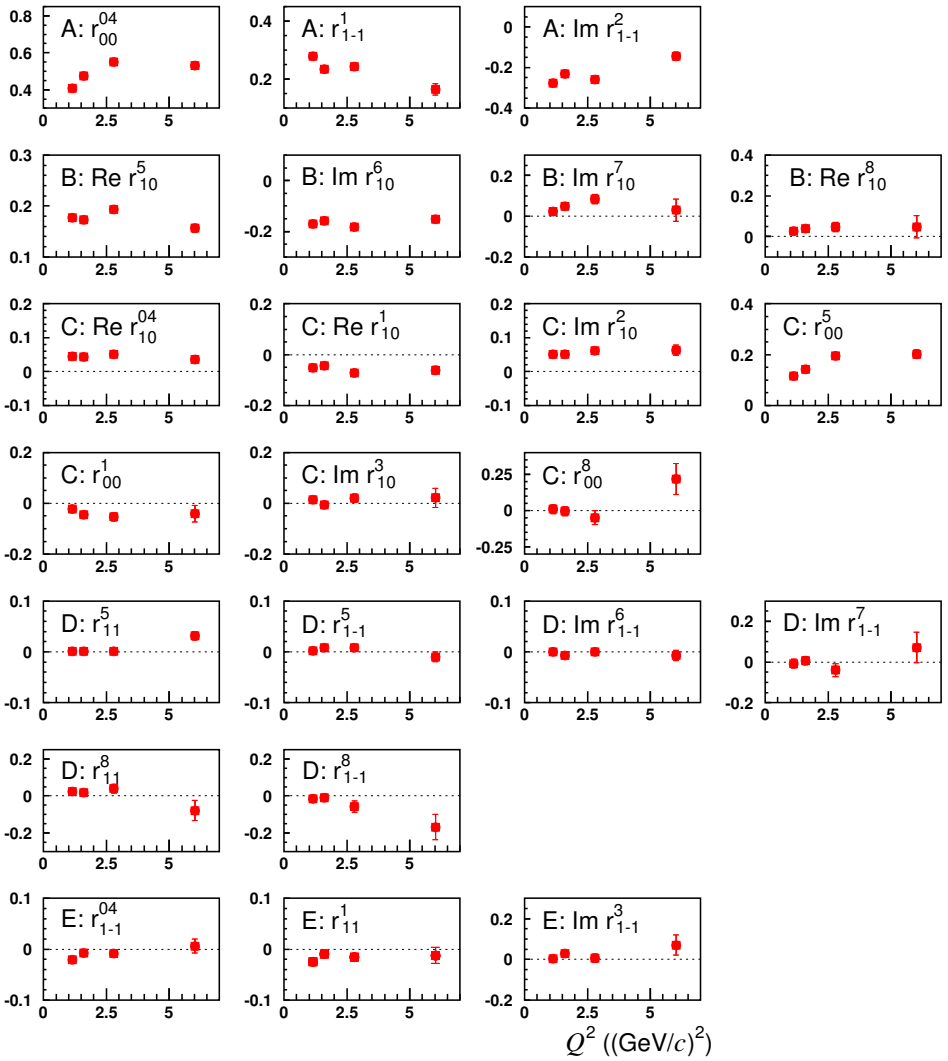

Fig. 5: Q^2 dependence of the measured 23 SDMEs. The capital letters A to E denote the class, to which the SDME belongs. Inner error bars represent statistical uncertainties and outer ones statistical and systematic uncertainties added in quadrature.

7 Discussion

7.1 Test of the SCHC hypothesis

In the case of SCHC only three amplitudes, T_{00}, T_{11} and U_{11}, may be different from zero. As a consequence all SDMEs of classes A and B may not vanish, while SDMEs from classes C, D, and E should be equal to zero. Six of the SDMEs in classes A and B have to fulfil the following relations [1]

$$\begin{aligned} r^1_{1-1} &= -\mathrm{Im}\{r^2_{1-1}\}, \\ \mathrm{Re}\{r^5_{10}\} &= -\mathrm{Im}\{r^6_{10}\}, \\ \mathrm{Im}\{r^7_{10}\} &= \mathrm{Re}\{r^8_{10}\}. \end{aligned} \tag{27}$$

Using the extracted SDMEs one obtains:

$$\begin{aligned} r^1_{1-1} + \mathrm{Im}\{r^2_{1-1}\} &= 0.000 \pm 0.006, \\ \mathrm{Re}\{r^5_{10}\} + \mathrm{Im}\{r^6_{10}\} &= 0.011 \pm 0.003, \end{aligned}$$

Table 2: Kinematic binning and mean values for kinematic variables.

bin	$\langle Q^2 \rangle$	$\langle p_T^2 \rangle$	$\langle W \rangle$
$1.0\ (\text{GeV}/c)^2 < Q^2 < 1.3\ (\text{GeV}/c)^2$	$1.14\ (\text{GeV}/c)^2$	$0.192\ (\text{GeV}/c)^2$	$8.8\ \text{GeV}/c^2$
$1.3\ (\text{GeV}/c)^2 < Q^2 < 2.0\ (\text{GeV}/c)^2$	$1.60\ (\text{GeV}/c)^2$	$0.198\ (\text{GeV}/c)^2$	$8.8\ \text{GeV}/c^2$
$2.0\ (\text{GeV}/c)^2 < Q^2 < 4.0\ (\text{GeV}/c)^2$	$2.80\ (\text{GeV}/c)^2$	$0.200\ (\text{GeV}/c)^2$	$8.7\ \text{GeV}/c^2$
$4.0\ (\text{GeV}/c)^2 < Q^2 < 10.0\ (\text{GeV}/c)^2$	$6.02\ (\text{GeV}/c)^2$	$0.206\ (\text{GeV}/c)^2$	$8.9\ \text{GeV}/c^2$
bin	$\langle p_T^2 \rangle$	$\langle Q^2 \rangle$	$\langle W \rangle$
$0.01\ (\text{GeV}/c)^2 < p_T^2 < 0.1\ (\text{GeV}/c)^2$	$0.053\ (\text{GeV}/c)^2$	$2.56\ (\text{GeV}/c)^2$	$8.8\ \text{GeV}/c^2$
$0.1\ (\text{GeV}/c)^2 < p_T^2 < 0.2\ (\text{GeV}/c)^2$	$0.147\ (\text{GeV}/c)^2$	$2.61\ (\text{GeV}/c)^2$	$8.7\ \text{GeV}/c^2$
$0.2\ (\text{GeV}/c)^2 < p_T^2 < 0.3\ (\text{GeV}/c)^2$	$0.248\ (\text{GeV}/c)^2$	$2.66\ (\text{GeV}/c)^2$	$8.7\ \text{GeV}/c^2$
$0.3\ (\text{GeV}/c)^2 < p_T^2 < 0.5\ (\text{GeV}/c)^2$	$0.391\ (\text{GeV}/c)^2$	$2.70\ (\text{GeV}/c)^2$	$8.7\ \text{GeV}/c^2$
bin	$\langle W \rangle$	$\langle Q^2 \rangle$	$\langle p_T^2 \rangle$
$5.0\ \text{GeV}/c^2 < W < 7.3\ \text{GeV}/c^2$	$7.0\ \text{GeV}/c^2$	$2.90\ (\text{GeV}/c)^2$	$0.196\ (\text{GeV}/c)^2$
$7.3\ \text{GeV}/c^2 < W < 9.0\ \text{GeV}/c^2$	$8.1\ \text{GeV}/c^2$	$2.65\ (\text{GeV}/c)^2$	$0.201\ (\text{GeV}/c)^2$
$9.0\ \text{GeV}/c^2 < W < 12.0\ \text{GeV}/c^2$	$10.0\ \text{GeV}/c^2$	$2.51\ (\text{GeV}/c)^2$	$0.199\ (\text{GeV}/c)^2$
$12.0\ \text{GeV}/c^2 < W < 17.0\ \text{GeV}/c^2$	$13.5\ \text{GeV}/c^2$	$2.13\ (\text{GeV}/c)^2$	$0.180\ (\text{GeV}/c)^2$

$$\text{Im}\{r_{10}^7\} - \text{Re}\{r_{10}^8\} \quad = \quad 0.009 \pm 0.031,$$

where total uncertainties are quoted. While the measurements of the first and the third relation in Eq. (27) are consistent with the expectation, a tension is observed for the second relation, which may indicate a contribution of single-helicity-flip amplitudes. In the case of the first relation only the contributions from squared small double-helicity-flip amplitudes violate SCHC. For the two other relations the contributions that violate SCHC are related to small terms corresponding to the interference of two single-helicity-flip amplitudes as well as the interference of the helicity-conserving amplitude T_{00} and the double-helicity-flip amplitude T_{1-1}.

However, for the transitions $\gamma_T^* \to V_L$ of class C the non-zero values of five unpolarised SDMEs indicate a clear SCHC violation. In the GK model [14], these SDMEs are related to the chiral-odd GPDs H_T and $\bar{E}_T$ coupled to the higher-twist wave function of the meson. The kinematic dependences of these SDMEs, as presented in Section 6, may help to further constrain the model.

7.2 Contribution of the helicity-flip NPE amplitudes

The contributions of non-zero helicity-single-flip and helicity-double-flip amplitudes to the cross section can be quantified by the ratios τ_{ij} of the helicity-flip amplitudes T_{ij} to the square root of the sum of all amplitudes squared

$$\tau_{ij} = \frac{|T_{ij}|}{\sqrt{\mathcal{N}}}. \tag{28}$$

Here, the normalisation factor $\mathcal{N}$ is given by $\mathcal{N} = \mathcal{N}_T + \epsilon \mathcal{N}_L$ with

$$\mathcal{N}_T = \widetilde{\sum}(|T_{11}|^2 + |T_{01}|^2 + |T_{-11}|^2 + |U_{11}|^2 + |U_{01}|^2 + |U_{-11}|^2), \tag{29}$$

$$\mathcal{N}_L = \widetilde{\sum}(|T_{00}|^2 + 2|T_{10}|^2 + 2|U_{10}|^2). \tag{30}$$

The ratios τ_{ij} can be expressed in terms of SDMEs as shown in Ref. [22].

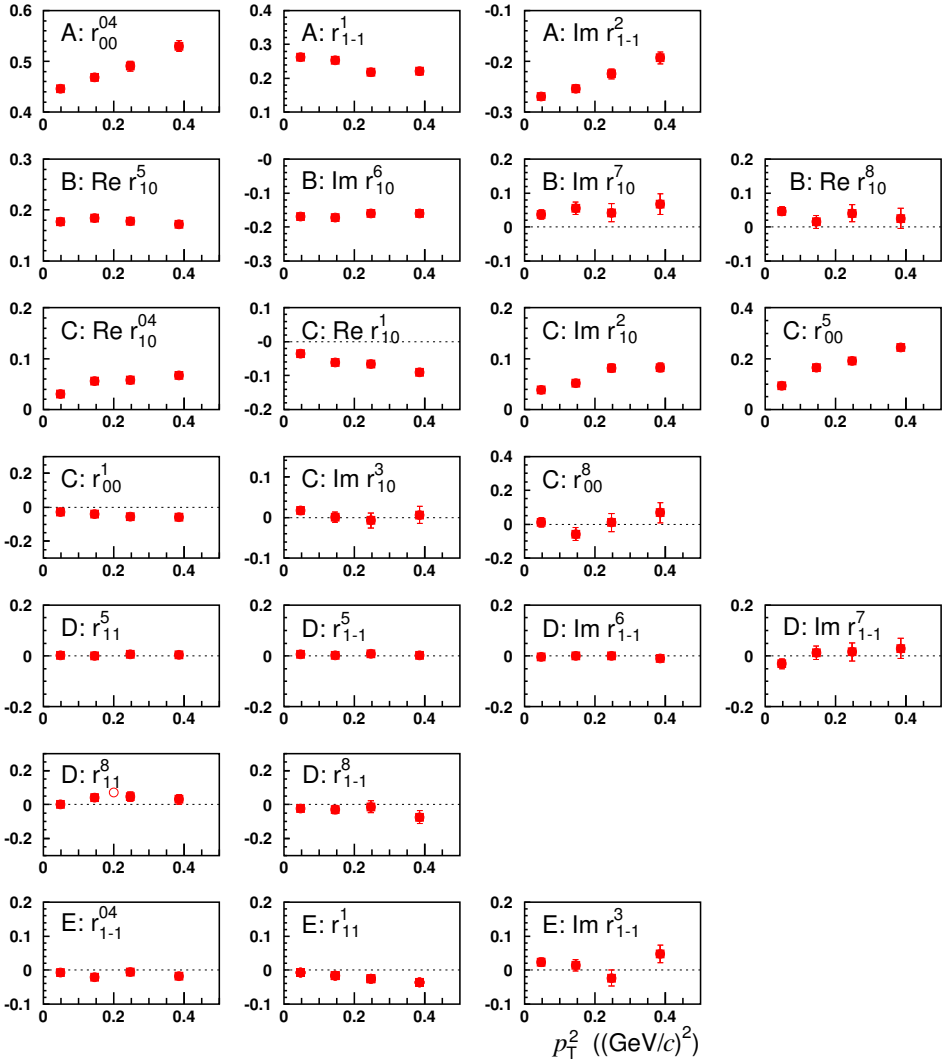

Fig. 6: p_T^2 dependence of the measured 23 SDMEs. The capital letters A to E denote the class, to which the SDME belongs. Inner error bars represent statistical uncertainties and outer ones statistical and systematic uncertainties added in quadrature.

For the amplitude T_{01} describing the transition $\gamma^*_T \to \rho^0_L$ the quantity τ_{01} is given by

$$\tau_{01} \approx \sqrt{\epsilon}\frac{\sqrt{(r^5_{00})^2 + (r^8_{00})^2}}{\sqrt{2r^{04}_{00}}}. \tag{31}$$

The quantity τ_{10}, which is related to the amplitude T_{10} describing the transition $\gamma^*_L \to \rho^0_T$, is approximated by

$$\tau_{10} \approx \frac{\sqrt{(r^5_{11} + \mathrm{Im}\{r^6_{1-1}\})^2 + (\mathrm{Im}\{r^7_{1-1}\} - r^8_{11})^2}}{\sqrt{2(r^1_{1-1} - \mathrm{Im}\{r^2_{1-1}\})}}. \tag{32}$$

For the helicity-double-flip amplitude T_{1-1} describing the transition $\gamma^*_{-T} \to \rho^0_T$ the quantity τ_{1-1} is given by

$$\tau_{1-1} \approx \frac{\sqrt{(r^1_{11})^2 + (\mathrm{Im}\{r^3_{1-1}\})^2}}{\sqrt{r^1_{1-1} - \mathrm{Im}\{r^2_{1-1}\}}}. \tag{33}$$

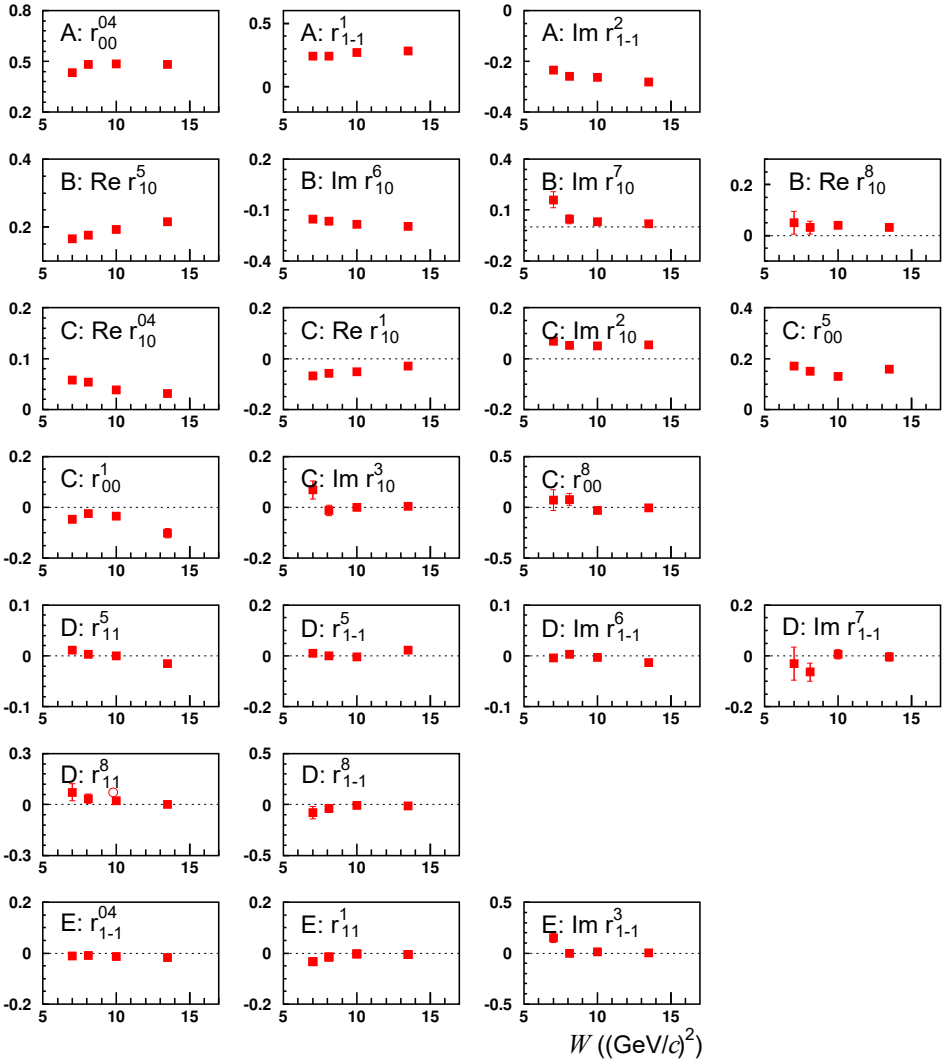

Fig. 7: W dependence of the measured 23 SDMEs. The capital letters A to E denote the class, to which the SDME belongs. Inner error bars represent statistical uncertainties and outer ones statistical and systematic uncertainties added in quadrature.

In Fig. 8 the dependence of the quantities τ_{01}, τ_{10} and τ_{1-1} on Q^2, p_T^2 and W is presented. For τ_{01}, values significantly different from zero are observed, while for τ_{10} and τ_{1-1} they are much smaller. This observation is consistent with the different degrees of SCHC violation seen for SDMEs in classes C, D and E.

A squared ratio τ^2_{ij} represents the fractional contribution from amplitude T_{ij} to the full cross section. Therefore the quantity

$$\tau^2_{\mathrm{NPE}} = (2\epsilon|T_{10}|^2 + |T_{01}|^2 + |T_{1-1}|^2)/\mathcal{N} \approx 2\epsilon\tau^2_{10} + \tau^2_{01} + \tau^2_{1-1} \tag{34}$$

represents the fractional contribution of helicity-flip NPE amplitudes to the cross section. The value of τ^2_{NPE} for the COMPASS entire kinematic range is small, equal to $0.023 \pm 0.002 \pm 0.004$.

7.3 UPE contribution in exclusive ρ^0 meson production

By examining a linear combination of SDMEs such as

$$u_1 = 1 - r^{04}_{00} + 2r^{04}_{1-1} - 2r^{1}_{11} - 2r^{1}_{1-1}\,, \tag{35}$$

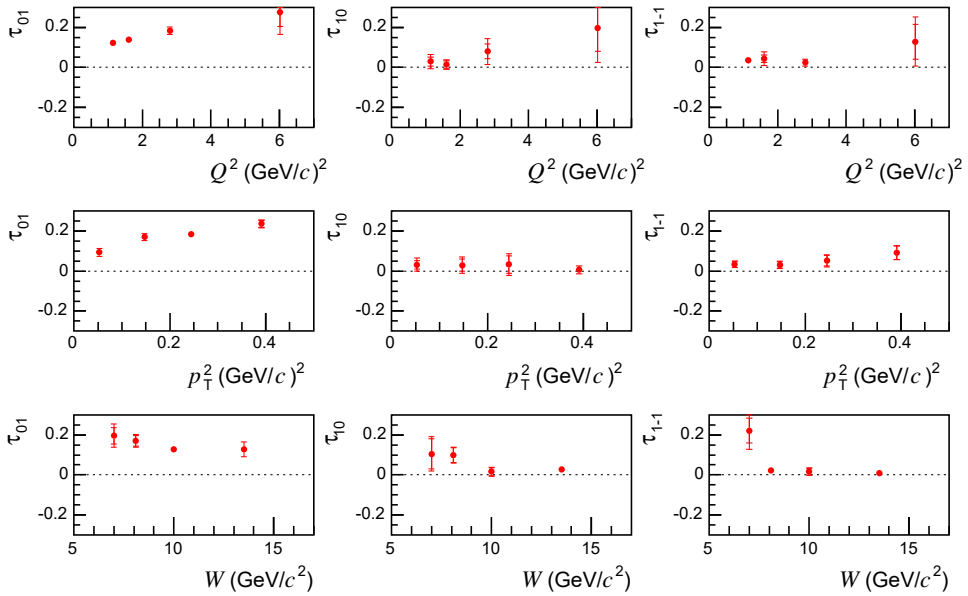

Fig. 8: Q^2, p_T^2 and W dependences of τ_{01}, τ_{10}, τ_{1-1}. Inner error bars represent statistical uncertainties and outer ones statistical and systematic uncertainties added in quadrature.

the presence of a UPE contribution can be tested. The quantity u_1 is expressed in terms of helicity amplitudes as

$$u_1 = \sum\!\!\!\!\!\!\sim \frac{4\epsilon|U_{10}|^2 + 2|U_{11} + U_{-11}|^2}{\mathcal{N}}, \tag{36}$$

thus a positive value of u_1 would indicate a non-zero contribution from UPE transitions. For the entire kinematic region of COMPASS u_1 is equal to $0.047 \pm 0.010 \pm 0.029$, which indicates a small UPE contribution. Additional information on UPE amplitudes can be obtained from the SDME combinations

$$u_2 = r^5_{11} + r^5_{1-1}, \tag{37}$$

$$u_3 = r^8_{11} + r^8_{1-1}, \tag{38}$$

which in terms of helicity amplitudes can be combined into

$$u_2 + \mathrm{i}u_3 = \sqrt{2}\sum\!\!\!\!\!\!\sim \frac{(\mathrm{U}_{11} + \mathrm{U}_{-11})\mathrm{U}^*_{10}}{\mathcal{N}}. \tag{39}$$

The value of $u_2 + \mathrm{i}u_3$ can vanish despite of the existence of UPE contributions. For COMPASS $u_2 = -0.008 \pm 0.002 \pm 0.013$ and $u_3 = -0.010 \pm 0.018 \pm 0.037$ are obtained, which are consistent with zero at the present accuracy of the data. In Fig. 9 the dependence of the quantities u_1, u_2 and u_3 on Q^2, p_T^2, and W is presented. The quantities u_1, u_2 and u_3 are small and compatible with zero within experimental uncertainties.

The UPE fractional contribution to the cross section is given as

$$\Delta_{\mathrm{UPE}} = (2\epsilon|U_{10}|^2 + |U_{01}|^2 + |U_{1-1}|^2 + |U_{11}|^2)/\mathcal{N} \approx u_1/2, \tag{40}$$

where the contributions of the amplitudes U_{01} and U_{1-1} was neglected for the approximate relation to u_1. The value of $\Delta_{\mathrm{UPE}}(\rho^0)$ for the entire kinematic range is $0.024 \pm 0.005 \pm 0.014$.

Altogether, for exclusive ρ^0 production at COMPASS the contribution of UPE is very small. This is in sharp contrast to the significant UPE contribution observed by COMPASS [31] for exclusive ω production in a similar kinematic range. There, this contribution is large over the entire kinematic range, $\Delta_{\mathrm{UPE}}(\omega)$

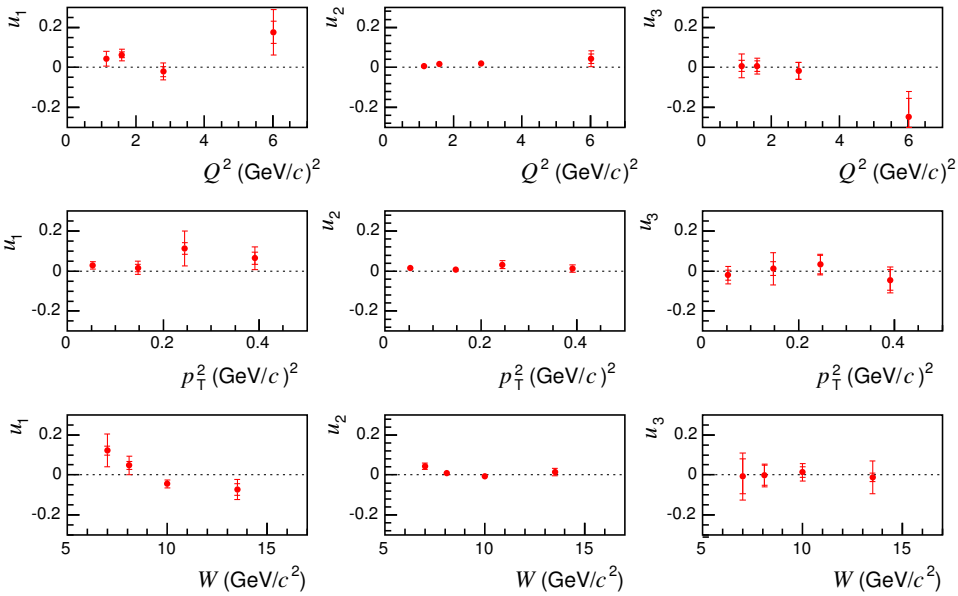

Fig. 9: Q^2, p_T^2, and W dependences of u_1, u_2, u_3. Inner error bars represent statistical uncertainties and outer ones statistical and systematic uncertainties added in quadrature.

= 0.415 ± 0.037 ± 0.025. The UPE dominates ω production at small W values and its contribution decreases with increasing W without vanishing towards large W values accessible in COMPASS. In the GK model, UPE is described by the GPDs $\widetilde{H}^f$ and $\widetilde{E}^f$ (non-pole), and by the pion-pole contribution treated as a one-boson exchange [16]. The large difference in size of the UPE contributions for ω and ρ^0 production is mostly explained by the difference between $\pi-\omega$ and $\pi-\rho^0$ transition form factors, with the former one being about three times larger than the latter [16].

7.4 The NPE-to-UPE asymmetry of the transverse cross section for the transition $\gamma_T^* \to V_T$

Another observable that is sensitive to the relative contributions of UPE and NPE amplitudes is the NPE-to-UPE asymmetry of the transverse differential cross section for the transition $\gamma_T^* \to V_T$. It is defined [16] as

$$P = \frac{d\sigma_T^N(\gamma_T^* \to V_T) - d\sigma_T^U(\gamma_T^* \to V_T)}{d\sigma_T^N(\gamma_T^* \to V_T) + d\sigma_T^U(\gamma_T^* \to V_T)} \approx \frac{2r^1_{1-1}}{1 - r^{04}_{00} - 2r^{04}_{1-1}}, \tag{41}$$

where the superscript N and U denotes the part of the cross section that is fed by NPE and UPE transitions, respectively.

The value of P obtained in the entire kinematic region is 0.887 ± 0.016 ± 0.029, which indicates that the NPE contribution dominates when averaged over the whole kinematic range of COMPASS. The kinematic dependences of the asymmetry P are shown in Fig. 10. A small UPE contribution is observed only at small values of W and it becomes compatible with zero at larger W. No significant Q^2 and p_T^2 dependences of the asymmetry are observed.

The COMPASS results for exclusive ω production [31] on the asymmetry P and its kinematic dependences exhibit a different behaviour. For the whole kinematic region the value is compatible with zero, $P(\omega)$ = −0.007 ± 0.076 ± 0.125, which indicates that the UPE and NPE contributions averaged over the whole kinematic range are of similar size. The UPE contribution dominates at small values of W and decreases with increasing W. At large values of W the NPE contribution for ω production becomes dominant, while a non-negligible UPE contribution still remains.

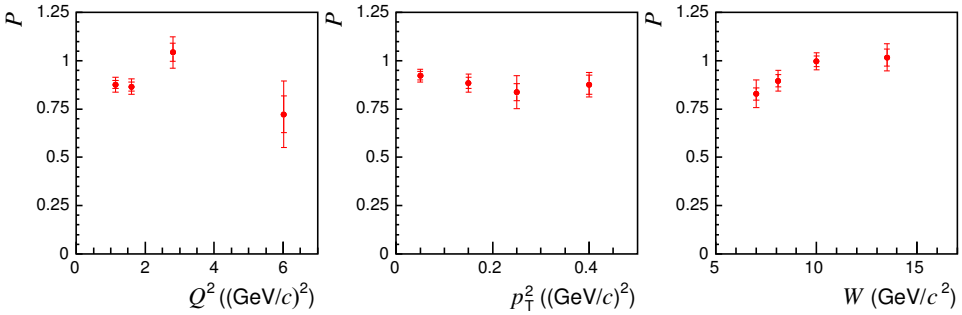

Fig. 10: Q^2, p_T^2 and W dependences of the NPE-to-UPE asymmetry of the transverse cross section for the transition $\gamma_T^* \to V_T$. Inner error bars represent statistical uncertainties and outer ones statistical and systematic uncertainties added in quadrature.

A semi-quantitative explanation of the difference between the values of asymmetry P measured for ρ^0 and ω production is possible by considering only the dominant contributions to the UPE and NPE cross sections for each process. In the framework of GK model such a contribution to the UPE cross sections is due to pion-pole exchange. Due to the difference between $\pi - \rho^0$ and $\pi - \omega$ transition form factors, which was mentioned in Sec. 7.3, the UPE cross section for ρ^0 is about 9 times smaller than that for ω production. For the NPE cross section, the dominant contribution is related to the gluon and sea-quark GPDs H and their relative contributions given in Ref. [47] imply that the cross section of exclusive ρ^0 production is about 9 times larger than that for ω. Taken together, UPE contributions are close to zero for ρ^0 and the P value approaches unity.

7.5 Longitudinal-to-transverse cross-section ratio

The longitudinal-to-transverse virtual-photon cross-section ratio

$$R = \frac{\sigma_L(\gamma_L^* \to V)}{\sigma_T(\gamma_T^* \to V)}, \tag{42}$$

is one of the most important observables in the study of light VM production since it is sensitive to the interaction dynamics. In order to evaluate R the quantity R' is commonly used:

$$R' = \frac{1}{\epsilon}\frac{r_{00}^{04}}{1 - r_{00}^{04}}. \tag{43}$$

Using expressions defining r_{00}^{04} and $1 - r_{00}^{04}$ in terms of helicity amplitudes [1, 22], the quantity R' may be interpreted [31] as longitudinal-to-transverse ratio of "effective" cross sections for the production of vector mesons that are polarised longitudinally or transversely irrespective of the virtual-photon polarisation. In case of SCHC, R' is equal to R. In spite of the observed violation of SCHC, the approximate relation $R \approx R'$ was used in most of the previous measurements. For the entire kinematic region, the ratio R' is found to be $0.980 \pm 0.014 \pm 0.089$. The kinematic dependences of R' are shown in Fig. 11.

In order to evaluate the effect of helicity-changing amplitudes on the estimate of the longitudinal-to-transverse cross-section ratio one can use a quantity $\widetilde{R}$ that is defined by following relation: [22]

$$\widetilde{R} = R' - \frac{\eta(1+\epsilon R')}{\epsilon(1+\eta)}, \tag{44}$$

where

$$\eta = \frac{(1+\epsilon R')}{N}\widetilde{\sum}\{|T_{01}|^2 + |U_{01}|^2 - 2\epsilon(|T_{10}|^2 + |U_{10}|^2)\}. \tag{45}$$

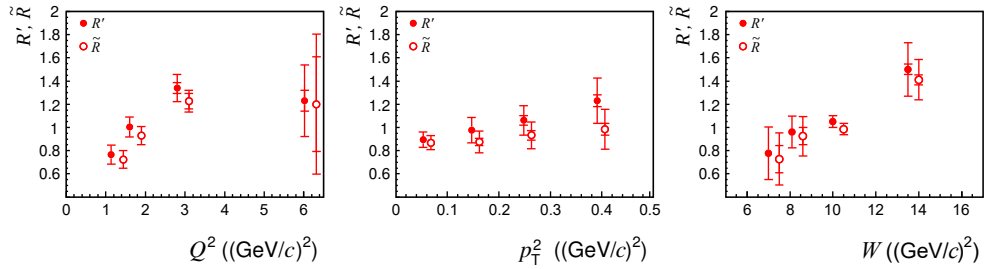

Fig. 11: Q^2, p_T^2 and W dependences of two estimates, R' and $\widetilde{R}$, of the longitudinal-to-transverse cross-section ratio R. Inner error bars represent statistical uncertainties and outer ones statistical and systematic uncertainties added in quadrature. For better visibility the data points for $\widetilde{R}$ are presented with a small horizontal off-set.

Table 3: Values of the ratios $\widetilde{R}$ and R' in kinematic bins and for the entire kinematic region. The first uncertainty values correspond to the statistical errors, and the second ones to the statistical and systematic uncertainties added in quadrature.

	$\widetilde{R}$	R'
$\langle Q^2 \rangle$		
$1.14\,(\mathrm{GeV}/c)^2$	$0.724 \pm 0.019 \pm 0.076$	$0.765 \pm 0.018 \pm 0.082$
$1.60\,(\mathrm{GeV}/c)^2$	$0.930 \pm 0.021 \pm 0.078$	$1.003 \pm 0.022 \pm 0.086$
$2.80\,(\mathrm{GeV}/c)^2$	$1.227 \pm 0.067 \pm 0.094$	$1.340 \pm 0.046 \pm 0.116$
$6.02\,(\mathrm{GeV}/c)^2$	$1.200 \pm 0.409 \pm 0.603$	$1.230 \pm 0.091 \pm 0.310$
$\langle p_T^2 \rangle$		
$0.053\,(\mathrm{GeV}/c)^2$	$0.868 \pm 0.020 \pm 0.061$	$0.894 \pm 0.018 \pm 0.067$
$0.147\,(\mathrm{GeV}/c)^2$	$0.874 \pm 0.030 \pm 0.094$	$0.977 \pm 0.028 \pm 0.110$
$0.248\,(\mathrm{GeV}/c)^2$	$0.932 \pm 0.042 \pm 0.114$	$1.061 \pm 0.041 \pm 0.127$
$0.391\,(\mathrm{GeV}/c)^2$	$0.984 \pm 0.051 \pm 0.173$	$1.230 \pm 0.052 \pm 0.195$
$\langle W \rangle$		
$7.0\,\mathrm{GeV}/c^2$	$0.728 \pm 0.118 \pm 0.225$	$0.779 \pm 0.026 \pm 0.227$
$8.1\,\mathrm{GeV}/c^2$	$0.924 \pm 0.075 \pm 0.171$	$0.961 \pm 0.027 \pm 0.138$
$10.0\,\mathrm{GeV}/c^2$	$0.986 \pm 0.025 \pm 0.049$	$1.051 \pm 0.025 \pm 0.049$
$13.5\,\mathrm{GeV}/c^2$	$1.411 \pm 0.043 \pm 0.175$	$1.501 \pm 0.045 \pm 0.232$
Entire range	$0.907 \pm 0.014 \pm 0.076$	$0.980 \pm 0.014 \pm 0.090$

The quantity η can be approximately estimated as

$$\eta \approx (1+\epsilon R')(\tau_{01}^2 - 2\epsilon\tau_{10}^2). \tag{46}$$

Here τ_{01} and τ_{10} are evaluated using Eqs. (31) and (32), and the small contributions of the helicity-flip UPE amplitudes U_{01} and U_{10} in Eq. (45) are neglected. In order to estimate the statistical uncertainty of $\widetilde{R}$, the SDMEs entering Eqs. (44) and (46) as well as their covariance matrix were used.

For the entire kinematic region the ratio $\widetilde{R}$ is found to be $0.907 \pm 0.014 \pm 0.074$. The values of $\widetilde{R}$ as functions of kinematic variables are shown in Fig. 11 for comparison with R'. The values of $\widetilde{R}$ and R' with their statistical and total uncertainties are also given in Table 3 for the kinematic bins and for the entire kinematic region. The total uncertainties for both observables are dominated by the systematic ones, which are similar for both cases. The additional unidirectional systematic error on R', which is due to the assumption of SCHC, is estimated from $\widetilde{R} - R'$ and is about -0.07 on average. Thus for an estimate

of the ratio R (defined by Eq. (42)) it is preferable to use the quantity $\widetilde{R}$, *i.e.* $R \approx \widetilde{R}$, while R' values may be used when comparing to earlier measurements that assumed SCHC.

A strong increase of the σ_L/σ_T ratio with increasing Q^2 is observed, while the p_T^2 and W dependences are weaker (see Fig. 11). The Q^2 dependence of R indicates that σ_L becomes dominant at Q^2 larger than about 2 $(\mathrm{GeV}/c)^2$.

7.6 Phase difference between amplitudes T_{11} and T_{00}

The phase difference between the amplitudes T_{11} and T_{00} can be evaluated as follows [22]:

$$\cos\delta = \frac{2\sqrt{\epsilon}(\mathrm{Re}\{r^5_{10}\} - \mathrm{Im}\{r^6_{10}\})}{\sqrt{r^{04}_{00}(1 - r^{04}_{00} + r^1_{1-1} - \mathrm{Im}\{r^2_{1-1}\})}}. \tag{47}$$

The result is $|\delta| = 19.6 \pm 0.9 \pm 3.9$ degrees. The sign of δ can be obtained from $\sin\delta$ [22] that depends on the polarised SDMEs:

$$\sin\delta = \frac{2\sqrt{\epsilon}(\mathrm{Re}\{r^8_{10}\} + \mathrm{Im}\{r^7_{10}\})}{\sqrt{r^{04}_{00}(1 - r^{04}_{00} + r^1_{1-1} - \mathrm{Im}\{r^2_{1-1}\})}}. \tag{48}$$

Using Eq. (48) one determines that the sign of δ is positive and $\delta = 12.9 \pm 2.1 \pm 0.8$ degrees. Both results on δ are compatible within large total uncertainties. As the final result we quote $\delta = 19.6 \pm 0.9 \pm 3.9$ degrees.

8 Comparison to other experiments

We compare the COMPASS results on SDMEs and related observables to those from the experiments that measured extensive sets of SDMEs for exclusive ρ^0 electroproduction: the HERMES [22], H1 [25, 26] and ZEUS [28, 29] experiments. Only the HERMES experiment measured the complete set of 15 unpolarised and 8 polarised SDMEs, while H1 and ZEUS measured 15 unpolarised SDMEs. Compilations of selected SDMEs-related observables, including other experiments, can be found *e.g.* in Refs. [22, 26].

The complete sets of SDMEs from HERMES and COMPASS for their entire kinematic ranges are compared in Fig. 12. The kinematic range for HERMES is 1.0 $(\mathrm{GeV}/c)^2 < Q^2 < 7.0$ $(\mathrm{GeV}/c)^2$, 3.0 $\mathrm{GeV}/c^2 < W < 6.3$ GeV/c^2, $|t'| < 0.4$ $(\mathrm{GeV}/c)^2$, while that for COMPASS 1.0 $(\mathrm{GeV}/c)^2 < Q^2 < 10.0$ $(\mathrm{GeV}/c)^2$, 5.0 $\mathrm{GeV}/c^2 < W < 17.0$ GeV/c^2, 0.01 $(\mathrm{GeV}/c)^2 < p_T^2 < 0.5$ $(\mathrm{GeV}/c)^2$. The ranges of Q^2 and the momentum transferred to the recoil proton are similar, but the W ranges overlap only marginally and the COMPASS range extends significantly towards large W values. In consequence, the contribution of gluons and sea quarks involved in exclusive meson production is higher by a factor of about 2.5 in COMPASS, while the remaining contribution (from valence quarks and interference terms) is a little smaller than in HERMES (see *e.g.* Ref. [48]). Significant differences are observed for the SDME r^{04}_{00}, which is proportional to the square of the leading helicity-conserving amplitude T_{00}, and for the unpolarised SDMEs from class C.

A more detailed comparison of selected observables in similar kinematic ranges for both experiments is presented in Table 4. The published HERMES results for the entire kinematic range ($\langle W\rangle = 4.8$ GeV/c^2) are compared to the COMPASS results for the lowest W bin ($\langle W\rangle = 7.0$ GeV/c^2). The quoted uncertainties are the total ones. For most of the observables the results from both experiments are compatible within one standard deviation, except τ_{01} and τ_{1-1}, for which the agreement is within two standard deviations.

The comparison of the Q^2 dependence of R between COMPASS and HERMES is not straightforward because the results are integrated over different W ranges for each experiment. Despite the moderate W dependence of R observed by COMPASS (*cf* Fig. 11), the estimates of R from both experiments are compatible within experimental uncertainties as shown in Fig. 13.

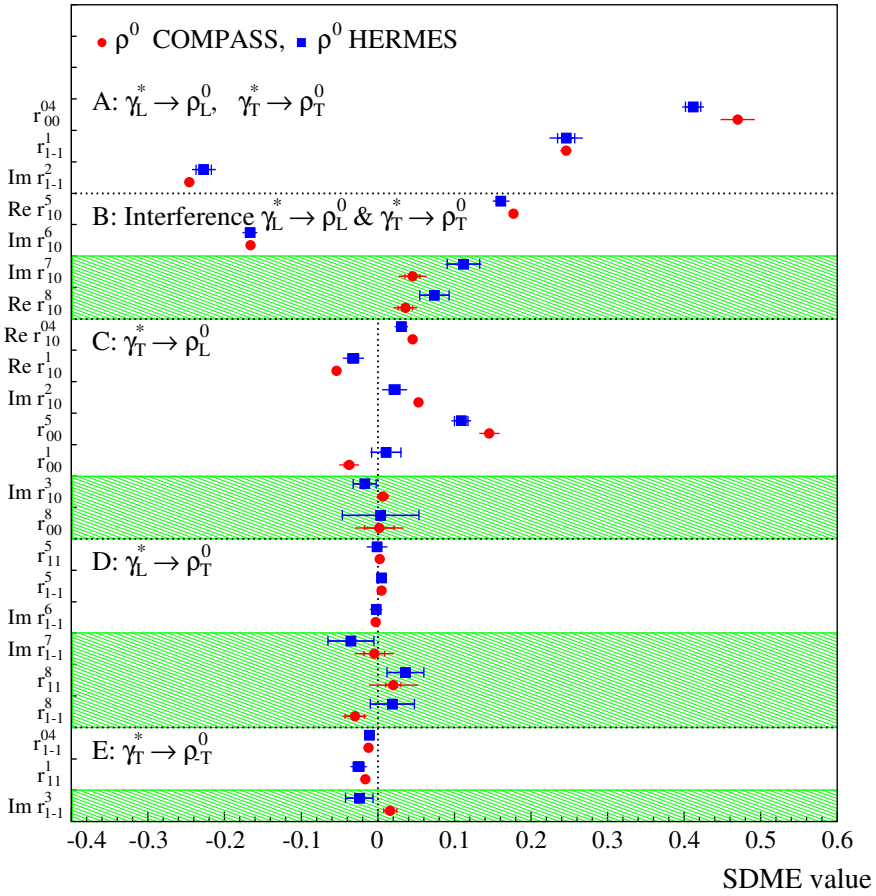

Fig. 12: Comparison of the 23 SDMEs for exclusive ρ^0 leptoproduction on the proton extracted in the entire kinematic regions of the HERMES and COMPASS experiments. For HERMES the average kinematic values are $\langle Q^2 \rangle = 1.96$ (GeV/c)^2, $\langle W \rangle = 4.8$ GeV/c^2, $\langle |t'| \rangle = 0.13$, while those for COMPASS are $\langle Q^2 \rangle = 2.40$ (GeV/c)^2, $\langle W \rangle = 9.9$ GeV/c^2, $\langle p_T^2 \rangle = 0.18$ (GeV/c)^2. Inner error bars represent statistical uncertainties and outer ones statistical and systematic uncertainties added in quadrature. Unpolarised (polarised) SDMEs are displayed in unshaded (shaded) areas.

The measurements of SDMEs for exclusive ρ^0 electroproduction by the ZEUS and H1 experiments were obtained in wide ranges of Q^2 and W at the highest available energies. Here, for comparison with COMPASS we use the ZEUS and H1 results from Refs. [25, 28]. The covered kinematic range for the DIS sample presented by the ZEUS experiment is 3 (GeV/c)^2 $< Q^2 <$ 30 (GeV/c)^2, 40 GeV/c^2 $< W <$ 120 GeV/c^2 and $|t| < 0.6$ (GeV/c)^2, while for H1 it is 1 (GeV/c)^2 $< Q^2 <$ 60 (GeV/c)^2, 30 GeV/c^2 $< W <$ 140 GeV/c^2 and $|t| < 0.5$ (GeV/c)^2. In this kinematic range the value of the virtual-photon polarisation parameter ϵ is close to 1 and the angular distribution for vector meson production and decay has a limited sensitivity to the polarised SDMEs (*cf.* Eq. 19). Thus the HERA experiments could measure only the 15 unpolarised SDMEs.

Deviations from zero are observed for five unpolarised SDMEs from classes A and B, which depend on the helicity-conserving amplitudes T_{00} and T_{11}. All other SDMEs are compatible with zero except r^5_{00}, which indicates the violation of SCHC for $\gamma^*_T \to \rho^0_L$ transitions. In order to quantify the size of SCHC violation, the ratios

$$\tilde{\tau}_{ij} = \frac{|T_{ij}|}{\sqrt{|T_{00}|^2 + |T_{11}|^2}} \tag{49}$$

were evaluated. The approximate expressions for $\tilde{\tau}_{ij}$ are given in Ref. [28]. In contrast to Eqs. (31, 32,

Table 4: Comparison of selected observables measured by HERMES and COMPASS in similar kinematic regions. The HERMES results for the proton target are integrated over the entire kinematic region. The COMPASS results are given for $5.0 < W < 7.3$ GeV/c^2. The total uncertainties are given.

Observable	HERMES - p $\langle W \rangle = 4.8$ GeV/c^2 $\langle Q^2 \rangle = 1.98$ (GeV/c)^2	COMPASS $\langle W \rangle = 7.0$ GeV/c^2 $\langle Q^2 \rangle = 2.90$ (GeV/c)^2
r_{00}^{04}	0.412 ± 0.014	0.435 ± 0.064
τ_{01}	0.114 ± 0.012	0.196 ± 0.059
τ_{10}	0.075 ± 0.030	0.105 ± 0.085
τ_{1-1}	0.051 ± 0.031	0.222 ± 0.092
u_1	0.125 ± 0.054	0.122 ± 0.085
u_2	-0.011 ± 0.013	0.022 ± 0.063
u_3	0.055 ± 0.045	-0.008 ± 0.116

33) those expressions rely on the assumptions of zero phase difference between the considered amplitude T_{ij} and the corresponding dominant amplitude (T_{00} or T_{11}), neglecting UPE contributions and assuming $\epsilon = 1$. For the kinematic ranges of the HERA experiments the values of $\tilde{\tau}_{01}$ are equal to 0.079 ± 0.026 for ZEUS and 0.08 ± 0.03 for H1, while the values of $\tilde{\tau}_{10}$ and $\tilde{\tau}_{1-1}$ are compatible with zero within experimental uncertainties. These results indicate that the helicity-flip amplitude T_{01} does not vanish even at the highest available energies. The comparison to the COMPASS result for the entire kinematic region, $\tau_{01} = 0.143 \pm 0.011$, indicates that the relative contribution of the amplitude T_{01} to the cross section becomes smaller for HERA kinematics.

Using Eqs. (36, 37) and the published ZEUS and H1 results on SDMEs for the entire kinematic range of each experiment [25, 28], one obtains the values of the u_1 and u_2 observables (u_3 is not available at HERA), which are related to the UPE contributions. The values of u_1 are equal to 0.091 ± 0.078 for ZEUS and 0.058 ± 0.125 for H1. The quoted uncertainties correspond to the quadratic sum of statistical and systematic uncertainties of individual SDMEs in Eq. (36) without taking into account the covariance matrix. Both values are consistent with zero within less than 1.5 standard deviations, similar to the COMPASS result (see Sec. 7.3). The HERMES result for u_1 indicates a slightly larger UPE contribution at small W values within 2.5 standard deviations from zero. The values of u_2 are very small (0.015 ± 0.016 for ZEUS and 0.004 ± 0.022 for H1) and compatible with zero. In addition, the H1 measurements of the NPE-to-UPE asymmetry P [26] as a function of Q^2 and $|t|$ are compatible with unity, which supports NPE for transversely polarised virtual-photons. The HERA results on both u_1 and P are consistent with the dominance of two-gluon exchange at high energy, which implies NPE.

The ZEUS and H1 results obtained from the large data sets of the 1996 – 2000 data-taking period were published in Refs. [26, 29], in which the Q^2, W, $|t|$ and $M_{\pi\pi}$ dependences of the cross section and SDMEs are discussed. The detailed discussion of SDME-related quantities focuses mainly on r_{00}^{04} and $R = \sigma_L/\sigma_T$. The values of both quantities increase with increasing Q^2 in the whole covered range up to $Q^2 \approx 40$ (GeV/c)^2. The strong increase at small Q^2 becomes milder at large Q^2. At Q^2 values larger than ≈ 10 (GeV/c)^2 the r_{00}^{04} values are larger than 0.75, which indicates the predominant contribution to the cross section from longitudinal virtual photons. Within experimental uncertainties no W dependence of r_{00}^{04} and R is observed by the two experiments, and in the case of ZEUS no $|t|$ dependence is seen.

In Fig. 13 the COMPASS results on the Q^2 dependence of R are compared to the previous experiments using results with $Q^2 > 1.0$ (GeV/c)^2 and with moderate to large values of W. The HERMES and COMPASS results are corrected for contributions of the spin-flip amplitudes T_{01} and T_{10}. For those from

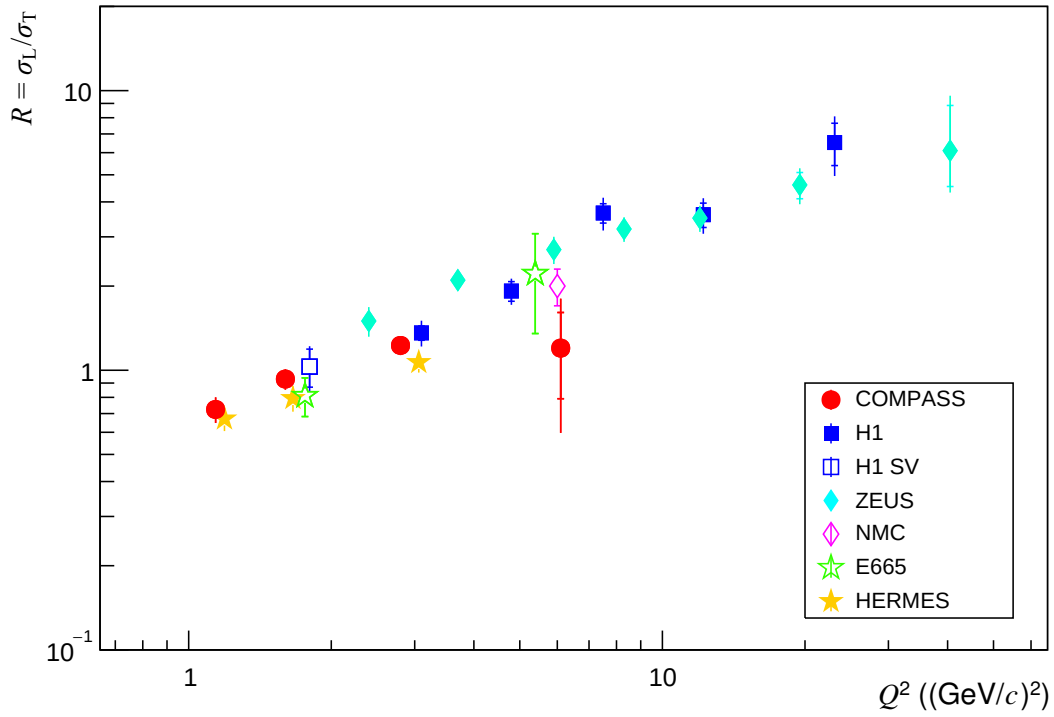

Fig. 13: The ratio $R = \sigma_L/\sigma_T$ as a function of Q^2. For comparison measurements of exclusive ρ^0 leptoproduction by fixed target experiments (HERMES [22], NMC [23], E665 [24]) and by HERA collider experiments (ZEUS [29], H1 [26], H1 SV [25]) are also shown.

H1 the contribution of T_{01} is taken into account, whereas the SCHC approximation is used for the other data. Despite small differences due to different treatments of small contributions of spin-flip amplitudes, and also due to a possible weak W dependence, all the results consistently show a main characteristic feature, *i.e.* the fast increase of R as a function of Q^2 within the wide energy range, from the fixed target experiments to the HERA collider measurements.

In LO pQCD and for $t = 0$ the ratio R is predicted to be $R = Q^2/M_V^2$ [45], where M_V is the mass of the produced vector meson. The experimental data on R for exclusive ρ^0, ϕ and J/ψ production confirm the scaling with M_V, but they lie systematically below this prediction (see, e.g., Fig. 38 from Ref. [26]). Deviations from this dependence, which become more pronounced as Q^2 increases, are due to effects of QCD evolution and quark transverse momentum [46, 47].

In the framework of the colour dipole model, different transverse sizes are predicted for virtual $q\bar{q}$ pair fluctuations originating from longitudinally and transversely polarised virtual photons, which leads to different kinematic dependences of σ_L, σ_T and R. The transverse size of these colour dipoles is on average smaller for longitudinal photons than for transverse ones. This results in a more shallow t (or p_T^2) dependence of the cross section for the longitudinal photons. In the unseparated cross section this effect leads to a decrease of the value of the t-slope parameter with increasing Q^2 (see *e.g.* Refs. [26, 29]).

9 Summary

Using exclusive ρ^0 meson muoproduction on the proton, we have measured 23 SDMEs at the average COMPASS kinematics, $\langle Q^2 \rangle = 2.4$ (GeV/c)^2, $\langle W \rangle = 9.9$ GeV/c^2 and $\langle p_T^2 \rangle = 0.18$ (GeV/c)^2. The SDMEs are extracted in the kinematic region 1.0 (GeV/c)^2 $< Q^2 <$ 10.0 (GeV/c)^2, 5.0 GeV/c^2 $< W <$ 17.0 GeV/c^2 and 0.01 (GeV/c)^2, $< p_T^2 <$ 0.5 (GeV/c)^2, which allows us to study their Q^2, p_T^2 and W dependences.

Several SDMEs that are depending on amplitudes describing $\gamma^*_T \to \rho^0_L$ transitions indicate a considerable violation of the SCHC hypothesis. These SDMEs are expected to be sensitive to the chiral-odd GPDs H_T and $\bar{E}_T$, which are coupled to the higher-twist wave function of the meson. A particularly prominent effect is observed for the SDME r^5_{00}, which strongly increases with increasing Q^2 and p^2_T.

Using specific observables that are constructed to be sensitive to the relative contributions from transitions with unnatural-parity exchanges, such as u_1 and the NPE-to-UPE asymmetry for the transverse cross section, we observe a dominance of NPE exchanges. The UPE contribution is very small and compatible with zero within experimental uncertainties.

The COMPASS results presented in this paper are obtained in the kinematic range that partially overlaps with the kinematic range of HERMES experimental data on SDMEs for exclusive ρ^0 electroproduction, but extends considerably towards higher W values. In the overlap region the results from both experiments are compatible. Important data on the behaviour of helicity amplitudes at very large values of Q^2 and W are provided by ZEUS and H1. Characteristic features are the dominant contribution of the amplitude describing the transition $\gamma^*_L \to \rho^0_L$, which increases with increasing Q^2, as well as negligible contributions of spin-flip and UPE amplitudes. These results allow one to better constrain extrapolations of trends observed at fixed target experiments.

The present results provide important input for modelling GPDs, in particular they may help to better constrain the chiral-odd GPDs and the amplitudes for UPE transitions in exclusive ρ^0 leptoproduction.

Acknowledgements

We are indebted to Sergey Goloskokov and Peter Kroll for numerous fruitful discussions on the interpretation of our results We gratefully acknowledge the support of CERN management and staff and the skill and effort of the technicians of our collaborating institutions.

Appendix

Table A.1 gives the various contributions to the systematic uncertainty of the 23 SDMEs and Tables A.2, A.3 and A.4 list their kinematic dependences.

Table A.1: Uncertainties for each SDME value: in column 3 the statistical uncertainty ("stat."), in columns 4–8 the individual contributions for each source of systematic uncertainty as defined in Section 5.3, in column 9 the total systematic uncertainty ("tot. sys."), and in column 10 the total uncertainty ("tot.").

SDME	value	stat.	beam charge (i)	$E_{\mathtt{miss}}$ (ii)	bg SDMEs (iii)	$f_{\mathtt{bg}}$ (iv)	simulation (v)	tot. sys.	tot.
r^{04}_{00}	0.470	0.004	0.007	0.009	0.019	−0.000	0.004	0.022	0.022
r^{1}_{1-1}	0.246	0.004	−0.003	0.003	−0.004	0.003	−0.001	0.006	0.007
Im r^{2}_{1-1}	−0.246	0.004	0.001	−0.001	0.004	−0.003	0.001	0.005	0.006
Re r^{5}_{10}	0.177	0.002	−0.002	0.002	−0.002	0.002	−0.001	0.004	0.004
Im r^{6}_{10}	−0.166	0.001	0.001	−0.001	0.003	−0.002	0.001	0.004	0.004
Im r^{7}_{10}	0.045	0.010	−0.016	−0.001	−0.001	0.001	0.000	0.016	0.018
Re r^{8}_{10}	0.036	0.010	0.012	−0.000	−0.001	0.000	0.000	0.012	0.015
Re r^{04}_{10}	0.045	0.002	0.001	0.003	0.005	0.000	0.001	0.006	0.006
Re r^{1}_{10}	−0.054	0.003	−0.000	−0.004	−0.000	−0.001	−0.001	0.004	0.005
Im r^{2}_{10}	0.053	0.003	0.003	0.003	−0.000	0.001	0.000	0.004	0.005
r^{5}_{00}	0.146	0.003	0.001	0.012	0.003	0.002	0.001	0.013	0.013
r^{1}_{00}	−0.038	0.006	−0.002	−0.011	0.001	−0.000	0.000	0.011	0.013
Im r^{3}_{10}	0.007	0.007	−0.004	0.001	−0.001	0.000	0.000	0.005	0.008
r^{8}_{00}	0.002	0.019	0.024	0.003	−0.008	0.000	−0.000	0.025	0.032
r^{5}_{11}	0.003	0.002	−0.002	0.001	0.001	−0.000	−0.000	0.003	0.003
r^{5}_{1-1}	0.005	0.002	0.002	−0.000	−0.001	0.000	−0.000	0.003	0.003
Im r^{6}_{1-1}	−0.003	0.002	−0.002	0.000	−0.001	−0.000	0.000	0.002	0.003
Im r^{7}_{1-1}	−0.005	0.013	0.021	−0.006	0.004	−0.000	−0.000	0.022	0.026
r^{8}_{11}	0.020	0.010	−0.030	−0.001	−0.001	0.000	−0.000	0.031	0.032
r^{8}_{1-1}	−0.030	0.013	−0.006	0.007	−0.001	−0.000	0.000	0.009	0.016
r^{04}_{1-1}	−0.012	0.003	−0.002	0.000	−0.003	−0.000	−0.000	0.003	0.004
r^{1}_{11}	−0.016	0.003	0.003	0.001	0.002	−0.000	−0.000	0.004	0.005
Im r^{3}_{1-1}	0.016	0.009	−0.004	0.001	0.002	0.000	−0.000	0.004	0.010

Table A.2: The measured 23 unpolarised and polarised ρ^0 SDMEs in bins of Q^2: 1.0 – 1.3 – 2.0 – 4.0 – 10.0 (GeV/c)^2. The first uncertainties are statistical, the second systematic.

SDME	$\langle Q^2 \rangle$ = 1.14 (GeV/c)^2	$\langle Q^2 \rangle$ = 1.60 (GeV/c)^2	$\langle Q^2 \rangle$ = 2.80 (GeV/c)^2	$\langle Q^2 \rangle$ = 6.02 (GeV/c)^2
r^{04}_{00}	$0.4080 \pm 0.0056 \pm 0.0243$	$0.4749 \pm 0.0055 \pm 0.0201$	$0.5490 \pm 0.0085 \pm 0.0193$	$0.5319 \pm 0.0183 \pm 0.0555$
r^{1}_{1-1}	$0.2781 \pm 0.0058 \pm 0.0088$	$0.2337 \pm 0.0057 \pm 0.0074$	$0.2437 \pm 0.0089 \pm 0.0061$	$0.1647 \pm 0.0193 \pm 0.0220$
Im r^{2}_{1-1}	$-0.2763 \pm 0.0060 \pm 0.0083$	$-0.2300 \pm 0.0059 \pm 0.0045$	$-0.2586 \pm 0.0089 \pm 0.0165$	$-0.1450 \pm 0.0199 \pm 0.0228$
Re r^{5}_{10}	$0.1774 \pm 0.0023 \pm 0.0042$	$0.1726 \pm 0.0023 \pm 0.0025$	$0.1938 \pm 0.0036 \pm 0.0083$	$0.1562 \pm 0.0078 \pm 0.0145$
Im r^{6}_{10}	$-0.1695 \pm 0.0021 \pm 0.0033$	$-0.1591 \pm 0.0023 \pm 0.0038$	$-0.1829 \pm 0.0035 \pm 0.0067$	$-0.1513 \pm 0.0077 \pm 0.0077$
Im r^{7}_{10}	$0.0230 \pm 0.0148 \pm 0.0158$	$0.0482 \pm 0.0152 \pm 0.0082$	$0.0851 \pm 0.0230 \pm 0.0343$	$0.0296 \pm 0.0553 \pm 0.0073$
Re r^{8}_{10}	$0.0253 \pm 0.0147 \pm 0.0111$	$0.0400 \pm 0.0146 \pm 0.0059$	$0.0466 \pm 0.0231 \pm 0.0365$	$0.0471 \pm 0.0548 \pm 0.0625$
Re r^{04}_{10}	$0.0452 \pm 0.0034 \pm 0.0058$	$0.0431 \pm 0.0034 \pm 0.0060$	$0.0508 \pm 0.0052 \pm 0.0069$	$0.0358 \pm 0.0110 \pm 0.0089$
Re r^{1}_{10}	$-0.0521 \pm 0.0044 \pm 0.0049$	$-0.0439 \pm 0.0045 \pm 0.0055$	$-0.0713 \pm 0.0070 \pm 0.0014$	$-0.0613 \pm 0.0150 \pm 0.0234$
Im r^{2}_{10}	$0.0505 \pm 0.0043 \pm 0.0031$	$0.0508 \pm 0.0045 \pm 0.0041$	$0.0612 \pm 0.0069 \pm 0.0060$	$0.0628 \pm 0.0151 \pm 0.0284$
r^{5}_{00}	$0.1150 \pm 0.0050 \pm 0.0080$	$0.1419 \pm 0.0052 \pm 0.0122$	$0.1950 \pm 0.0081 \pm 0.0213$	$0.2021 \pm 0.0167 \pm 0.0406$
r^{1}_{00}	$-0.0217 \pm 0.0092 \pm 0.0109$	$-0.0441 \pm 0.0097 \pm 0.0103$	$-0.0532 \pm 0.0156 \pm 0.0420$	$-0.0419 \pm 0.0326 \pm 0.0254$
Im r^{3}_{10}	$0.0144 \pm 0.0104 \pm 0.0027$	$-0.0068 \pm 0.0105 \pm 0.0084$	$0.0209 \pm 0.0161 \pm 0.0114$	$0.0212 \pm 0.0380 \pm 0.0694$
r^{8}_{00}	$0.0095 \pm 0.0302 \pm 0.0269$	$-0.0041 \pm 0.0304 \pm 0.0294$	$-0.0498 \pm 0.0477 \pm 0.0385$	$0.2174 \pm 0.1065 \pm 0.1142$
r^{5}_{11}	$0.0014 \pm 0.0026 \pm 0.0040$	$0.0009 \pm 0.0025 \pm 0.0017$	$0.0014 \pm 0.0037 \pm 0.0055$	$0.0316 \pm 0.0080 \pm 0.0230$
r^{5}_{1-1}	$0.0017 \pm 0.0032 \pm 0.0027$	$0.0079 \pm 0.0031 \pm 0.0054$	$0.0087 \pm 0.0047 \pm 0.0042$	$-0.0096 \pm 0.0100 \pm 0.0087$
Im r^{6}_{1-1}	$0.0006 \pm 0.0031 \pm 0.0025$	$-0.0074 \pm 0.0031 \pm 0.0027$	$0.0003 \pm 0.0046 \pm 0.0029$	$-0.0067 \pm 0.0102 \pm 0.0033$
Im r^{7}_{1-1}	$-0.0079 \pm 0.0215 \pm 0.0444$	$0.0063 \pm 0.0206 \pm 0.0086$	$-0.0400 \pm 0.0314 \pm 0.0156$	$0.0716 \pm 0.0755 \pm 0.0571$
r^{8}_{11}	$0.0227 \pm 0.0163 \pm 0.0310$	$0.0168 \pm 0.0156 \pm 0.0140$	$0.0397 \pm 0.0243 \pm 0.0562$	$-0.0800 \pm 0.0546 \pm 0.0492$
r^{8}_{1-1}	$-0.0154 \pm 0.0206 \pm 0.0209$	$-0.0105 \pm 0.0195 \pm 0.0177$	$-0.0575 \pm 0.0309 \pm 0.0569$	$-0.1683 \pm 0.0698 \pm 0.0418$
r^{04}_{1-1}	$-0.0213 \pm 0.0044 \pm 0.0055$	$-0.0074 \pm 0.0042 \pm 0.0030$	$-0.0081 \pm 0.0064 \pm 0.0073$	$0.0059 \pm 0.0136 \pm 0.0057$
r^{1}_{11}	$-0.0252 \pm 0.0051 \pm 0.0083$	$-0.0099 \pm 0.0049 \pm 0.0069$	$-0.0157 \pm 0.0074 \pm 0.0101$	$-0.0122 \pm 0.0159 \pm 0.0146$
Im r^{3}_{1-1}	$0.0038 \pm 0.0134 \pm 0.0110$	$0.0279 \pm 0.0131 \pm 0.0192$	$0.0051 \pm 0.0205 \pm 0.0094$	$0.0702 \pm 0.0495 \pm 0.0476$

Table A.3: The measured 23 unpolarised and polarised ρ^0 SDMEs in bins of p_T^2: 0.01 – 0.1 – 0.3 – 0.5 (GeV/c)^2. The first uncertainties are statistical, the second systematic.

SDME	$\langle p_T^2 \rangle$ = 0.053 (GeV/c)^2	$\langle p_T^2 \rangle$ = 0.147 (GeV/c)^2	$\langle p_T^2 \rangle$ = 0.248 (GeV/c)^2	$\langle p_T^2 \rangle$ = 0.391 (GeV/c)^2
r^{04}_{00}	$0.4458 \pm 0.0051 \pm 0.0173$	$0.4690 \pm 0.0070 \pm 0.0260$	$0.4906 \pm 0.0095 \pm 0.0273$	$0.5300 \pm 0.0105 \pm 0.0368$
r^{1}_{1-1}	$0.2626 \pm 0.0052 \pm 0.0080$	$0.2536 \pm 0.0072 \pm 0.0077$	$0.2177 \pm 0.0101 \pm 0.0197$	$0.2212 \pm 0.0109 \pm 0.0123$
Im r^{2}_{1-1}	$-0.2694 \pm 0.0053 \pm 0.0061$	$-0.2534 \pm 0.0075 \pm 0.0144$	$-0.2247 \pm 0.0101 \pm 0.0140$	$-0.1929 \pm 0.0115 \pm 0.0116$
Re r^{5}_{10}	$0.1774 \pm 0.0021 \pm 0.0035$	$0.1841 \pm 0.0029 \pm 0.0043$	$0.1777 \pm 0.0039 \pm 0.0059$	$0.1719 \pm 0.0046 \pm 0.0064$
Im r^{6}_{10}	$-0.1694 \pm 0.0021 \pm 0.0031$	$-0.1718 \pm 0.0028 \pm 0.0051$	$-0.1593 \pm 0.0039 \pm 0.0069$	$-0.1603 \pm 0.0042 \pm 0.0079$
Im r^{7}_{10}	$0.0368 \pm 0.0137 \pm 0.0125$	$0.0549 \pm 0.0181 \pm 0.0122$	$0.0420 \pm 0.0271 \pm 0.0425$	$0.0672 \pm 0.0301 \pm 0.0365$
Re r^{8}_{10}	$0.0467 \pm 0.0133 \pm 0.0094$	$0.0148 \pm 0.0188 \pm 0.0163$	$0.0402 \pm 0.0250 \pm 0.0147$	$0.0252 \pm 0.0298 \pm 0.0491$
Re r^{04}_{10}	$0.0307 \pm 0.0031 \pm 0.0076$	$0.0556 \pm 0.0042 \pm 0.0079$	$0.0578 \pm 0.0056 \pm 0.0089$	$0.0674 \pm 0.0064 \pm 0.0132$
Re r^{1}_{10}	$-0.0352 \pm 0.0041 \pm 0.0085$	$-0.0614 \pm 0.0057 \pm 0.0030$	$-0.0665 \pm 0.0074 \pm 0.0084$	$-0.0906 \pm 0.0089 \pm 0.0160$
Im r^{2}_{10}	$0.0383 \pm 0.0041 \pm 0.0072$	$0.0514 \pm 0.0054 \pm 0.0028$	$0.0817 \pm 0.0078 \pm 0.0095$	$0.0827 \pm 0.0086 \pm 0.0077$
r^{5}_{00}	$0.0929 \pm 0.0047 \pm 0.0184$	$0.1644 \pm 0.0065 \pm 0.0092$	$0.1920 \pm 0.0088 \pm 0.0100$	$0.2450 \pm 0.0096 \pm 0.0101$
r^{1}_{00}	$-0.0289 \pm 0.0088 \pm 0.0199$	$-0.0390 \pm 0.0120 \pm 0.0102$	$-0.0560 \pm 0.0167 \pm 0.0388$	$-0.0584 \pm 0.0185 \pm 0.0154$
Im r^{3}_{10}	$0.0171 \pm 0.0095 \pm 0.0060$	$0.0011 \pm 0.0128 \pm 0.0090$	$-0.0072 \pm 0.0186 \pm 0.0231$	$0.0060 \pm 0.0208 \pm 0.0041$
r^{8}_{00}	$0.0122 \pm 0.0274 \pm 0.0520$	$-0.0578 \pm 0.0382 \pm 0.0446$	$0.0098 \pm 0.0525 \pm 0.0430$	$0.0676 \pm 0.0610 \pm 0.0290$
r^{5}_{11}	$0.0017 \pm 0.0023 \pm 0.0066$	$0.0006 \pm 0.0032 \pm 0.0022$	$0.0070 \pm 0.0043 \pm 0.0051$	$0.0050 \pm 0.0047 \pm 0.0103$
r^{5}_{1-1}	$0.0060 \pm 0.0028 \pm 0.0030$	$0.0031 \pm 0.0039 \pm 0.0015$	$0.0093 \pm 0.0054 \pm 0.0027$	$0.0013 \pm 0.0059 \pm 0.0126$
Im r^{6}_{1-1}	$-0.0037 \pm 0.0028 \pm 0.0038$	$0.0009 \pm 0.0039 \pm 0.0022$	$0.0006 \pm 0.0051 \pm 0.0087$	$-0.0107 \pm 0.0056 \pm 0.0048$
Im r^{7}_{1-1}	$-0.0309 \pm 0.0191 \pm 0.0568$	$0.0121 \pm 0.0265 \pm 0.0373$	$0.0159 \pm 0.0362 \pm 0.0595$	$0.0293 \pm 0.0403 \pm 0.0224$
r^{8}_{11}	$0.0020 \pm 0.0145 \pm 0.0364$	$0.0418 \pm 0.0200 \pm 0.0332$	$0.0459 \pm 0.0277 \pm 0.0066$	$0.0301 \pm 0.0301 \pm 0.0401$
r^{8}_{1-1}	$-0.0222 \pm 0.0182 \pm 0.0044$	$-0.0296 \pm 0.0252 \pm 0.0409$	$-0.0131 \pm 0.0346 \pm 0.0203$	$-0.0750 \pm 0.0380 \pm 0.0204$
r^{04}_{1-1}	$-0.0075 \pm 0.0039 \pm 0.0033$	$-0.0210 \pm 0.0053 \pm 0.0041$	$-0.0055 \pm 0.0073 \pm 0.0038$	$-0.0173 \pm 0.0079 \pm 0.0105$
r^{1}_{11}	$-0.0075 \pm 0.0046 \pm 0.0010$	$-0.0170 \pm 0.0063 \pm 0.0045$	$-0.0253 \pm 0.0084 \pm 0.0172$	$-0.0360 \pm 0.0091 \pm 0.0059$
Im r^{3}_{1-1}	$0.0234 \pm 0.0121 \pm 0.0026$	$0.0138 \pm 0.0168 \pm 0.0092$	$-0.0236 \pm 0.0236 \pm 0.0049$	$0.0473 \pm 0.0261 \pm 0.0047$

Table A.4: The measured 23 unpolarised and polarised ρ^0 SDMEs in bins of W: $5.00 - 7.3 - 9.0 - 12.0 - 17.0$ GeV/c^2. The first uncertainties are statistical, the second systematic.

SDME	$\langle W \rangle$ = 7.0 GeV/c^2	$\langle W \rangle$ = 8.1 GeV/c^2	$\langle W \rangle$ = 10.0 GeV/c^2	$\langle W \rangle$ = 13.5 GeV/c^2
r^{04}_{00}	$0.4349 \pm 0.0083 \pm 0.0639$	$0.4819 \pm 0.0070 \pm 0.0335$	$0.4862 \pm 0.0059 \pm 0.0100$	$0.4836 \pm 0.0074 \pm 0.0356$
r^{1}_{1-1}	$0.2432 \pm 0.0080 \pm 0.0165$	$0.2409 \pm 0.0070 \pm 0.0096$	$0.2689 \pm 0.0060 \pm 0.0054$	$0.2808 \pm 0.0111 \pm 0.0288$
Im r^{2}_{1-1}	$-0.2344 \pm 0.0083 \pm 0.0081$	$-0.2587 \pm 0.0069 \pm 0.0081$	$-0.2627 \pm 0.0063 \pm 0.0045$	$-0.2804 \pm 0.0117 \pm 0.0192$
Re r^{5}_{10}	$0.1659 \pm 0.0035 \pm 0.0110$	$0.1762 \pm 0.0028 \pm 0.0071$	$0.1927 \pm 0.0024 \pm 0.0042$	$0.2149 \pm 0.0041 \pm 0.0105$
Im r^{6}_{10}	$-0.1539 \pm 0.0033 \pm 0.0128$	$-0.1671 \pm 0.0028 \pm 0.0082$	$-0.1849 \pm 0.0023 \pm 0.0035$	$-0.1978 \pm 0.0039 \pm 0.0134$
Im r^{7}_{10}	$0.1599 \pm 0.0472 \pm 0.0535$	$0.0451 \pm 0.0259 \pm 0.0133$	$0.0302 \pm 0.0122 \pm 0.0264$	$0.0191 \pm 0.0108 \pm 0.0106$
Re r^{8}_{10}	$0.0502 \pm 0.0454 \pm 0.0840$	$0.0313 \pm 0.0254 \pm 0.0068$	$0.0390 \pm 0.0121 \pm 0.0105$	$0.0314 \pm 0.0104 \pm 0.0137$
Re r^{04}_{10}	$0.0584 \pm 0.0049 \pm 0.0176$	$0.0540 \pm 0.0042 \pm 0.0081$	$0.0388 \pm 0.0037 \pm 0.0059$	$0.0318 \pm 0.0048 \pm 0.0039$
Re r^{1}_{10}	$-0.0685 \pm 0.0065 \pm 0.0135$	$-0.0572 \pm 0.0055 \pm 0.0041$	$-0.0521 \pm 0.0048 \pm 0.0063$	$-0.0285 \pm 0.0090 \pm 0.0093$
Im r^{2}_{10}	$0.0684 \pm 0.0064 \pm 0.0055$	$0.0514 \pm 0.0054 \pm 0.0104$	$0.0502 \pm 0.0045 \pm 0.0097$	$0.0551 \pm 0.0079 \pm 0.0179$
r^{5}_{00}	$0.1704 \pm 0.0071 \pm 0.0162$	$0.1505 \pm 0.0062 \pm 0.0056$	$0.1291 \pm 0.0057 \pm 0.0112$	$0.1589 \pm 0.0089 \pm 0.0508$
r^{1}_{00}	$-0.0478 \pm 0.0138 \pm 0.0204$	$-0.0252 \pm 0.0118 \pm 0.0122$	$-0.0346 \pm 0.0103 \pm 0.0135$	$-0.1018 \pm 0.0179 \pm 0.0648$
Im r^{3}_{10}	$0.0682 \pm 0.0359 \pm 0.0297$	$-0.0123 \pm 0.0206 \pm 0.0173$	$0.0003 \pm 0.0103 \pm 0.0080$	$0.0037 \pm 0.0076 \pm 0.0112$
r^{8}_{00}	$0.0694 \pm 0.1017 \pm 0.0879$	$0.0776 \pm 0.0570 \pm 0.0335$	$-0.0332 \pm 0.0278 \pm 0.0109$	$-0.0033 \pm 0.0225 \pm 0.0269$
r^{5}_{11}	$0.0118 \pm 0.0035 \pm 0.0111$	$0.0029 \pm 0.0030 \pm 0.0026$	$-0.0000 \pm 0.0027 \pm 0.0022$	$-0.0152 \pm 0.0044 \pm 0.0061$
r^{5}_{1-1}	$0.0101 \pm 0.0043 \pm 0.0067$	$0.0010 \pm 0.0037 \pm 0.0018$	$-0.0032 \pm 0.0032 \pm 0.0033$	$0.0221 \pm 0.0055 \pm 0.0051$
Im r^{6}_{1-1}	$-0.0035 \pm 0.0042 \pm 0.0061$	$0.0033 \pm 0.0036 \pm 0.0020$	$-0.0033 \pm 0.0034 \pm 0.0039$	$-0.0135 \pm 0.0054 \pm 0.0028$
Im r^{7}_{1-1}	$-0.0308 \pm 0.0653 \pm 0.0425$	$-0.0639 \pm 0.0354 \pm 0.0147$	$0.0071 \pm 0.0183 \pm 0.0167$	$-0.0039 \pm 0.0160 \pm 0.0335$
r^{8}_{11}	$0.0719 \pm 0.0499 \pm 0.0585$	$0.0352 \pm 0.0283 \pm 0.0075$	$0.0231 \pm 0.0149 \pm 0.0051$	$0.0019 \pm 0.0122 \pm 0.0370$
r^{8}_{1-1}	$-0.0800 \pm 0.0615 \pm 0.0288$	$-0.0379 \pm 0.0345 \pm 0.0244$	$-0.0090 \pm 0.0178 \pm 0.0369$	$-0.0135 \pm 0.0150 \pm 0.0430$
r^{04}_{1-1}	$-0.0110 \pm 0.0061 \pm 0.0098$	$-0.0097 \pm 0.0053 \pm 0.0059$	$-0.0125 \pm 0.0046 \pm 0.0058$	$-0.0179 \pm 0.0059 \pm 0.0089$
r^{1}_{11}	$-0.0326 \pm 0.0067 \pm 0.0091$	$-0.0153 \pm 0.0059 \pm 0.0087$	$-0.0023 \pm 0.0053 \pm 0.0064$	$-0.0042 \pm 0.0096 \pm 0.0067$
Im r^{3}_{1-1}	$0.1497 \pm 0.0445 \pm 0.0490$	$-0.0018 \pm 0.0240 \pm 0.0375$	$0.0117 \pm 0.0124 \pm 0.0038$	$0.0048 \pm 0.0096 \pm 0.0042$

References

[1] K. Schilling and G. Wolf, Nucl. Phys. B **61**, 381(1973).

[2] M. Diehl, JHEP **0709**, 064 (2007).

[3] R. Devenish and A. Cooper-Sarkar, "Deep Inelastic Scattering", p.263, Oxford University Press (2004).

[4] A.C. Irwing and R.P. Worden, Phys. Rep. **C34**, 117 (1977).

[5] D. Müller et al., Fortschr. Phys. **42**, 101 (1994).

[6] X. Ji, Phys. Rev. Lett. **78**, 610 (1997).

[7] X. Ji, Phys. Rev. D **55**, 7114 (1997).

[8] A.V. Radyushkin, Phys. Lett. B **385**, 333 (1996).

[9] A.V. Radyushkin, Phys. Rev. D **56**, 5524 (1997).

[10] J.C. Collins, L. Frankfurt, M. Strikman, Phys. Rev. D **56**, 2982 (1997).

[11] A.D. Martin, M.G. Ryskin, T. Teubner, Phys. Rev. **55**, 4329 (1997).

[12] S.V. Goloskokov, P. Kroll, Eur. Phys. J. C **42**, 281 (2005).

[13] S.V. Goloskokov, P. Kroll, Eur. Phys. J. C **53**, 367 (2008).

[14] S.V. Goloskokov, P. Kroll, Eur. Phys. J. C **59**, 809 (2009).

[15] S.V. Goloskokov, P. Kroll, Eur. Phys. J. C **74**, 2725 (2014).

[16] S.V. Goloskokov, P. Kroll, Eur. Phys. J. A **50**, 146 (2014).

[17] D.G. Cassel et al., Phys. Rev. D **24**, 2787 (1981).

[18] C. Hadjidakis et al. (CLAS Collaboration), Phys. Lett. B **605**, 256 (2005).

[19] S.A. Morrow et al. (CLAS Collaboration), Eur. Phys. J. A **39**, 5 (2009).

[20] A. Airapetian et al. (HERMES Collaboration), Eur. Phys. J. C **17**, 389 (2000).

[21] K. Ackerstaff et al. (HERMES Collaboration), Eur. Phys. J. C **18**, 303 (2000).

[22] A. Airapetian et al. (HERMES Collaboration), Eur. Phys. J. C **62**, 659 (2009).

[23] M. Arneodo et al. (New Muon Collaboration), Nucl. Phys. B **429**, 503 (1994).

[24] M.R. Adams et al., Z. Phys. C **74**, 237 (1997).

[25] C. Adloff et al. (H1 Collaboration), Eur. Phys. J. C **13**, 371 (2000).

[26] F.D. Aaron et al. (H1 Collaboration), JHEP **1005**, 032 (2010).

[27] J. Breitweg et al. (ZEUS Collaboration), Eur. Phys. J. C **6**, 603 (1999).

[28] J. Breitweg et al. (ZEUS Collaboration), Eur. Phys. J. C **12**, 393 (2000).

[29] S. Chekanov et al. (ZEUS Collaboration), PMC Phys. A **1**, 6 (2007).

[30] Ling-Lie Chau Wang, Phys. Rev. **142**, 1187 (1966).

[31] G.D. Alexeev et al. (COMPASS Collaboration), Eur. Phys. J. C **81**, 126 (2021).

[32] A. Airapetian et al. (HERMES Collaboration), Eur. Phys. J. C **74**, 3110 (2014); Erratum: Eur. Phys. J. C **76**, 162 (2016).

[33] P. Joos et al., Nucl. Phys. B **113**, 53 (1976).

[34] C. Adolph et al. (COMPASS Collaboration), Phys. Lett. B **731**, 19 (2014).

[35] P. Abbon et al. (COMPASS Collaboration), Nucl. Instrum. Meth. A **557**, 455 (2007).

[36] P. Abbon et al. (COMPASS Collaboration), Nucl. Instrum. Meth. A **779**, 69 (2015).

[37] F. Gautheron et al. (COMPASS Collaboration), SPSC-P-340, CERN-SPSC-2019-014.

[38] P. Sznajder, PhD thesis, National Centre For Nuclear Research, Otwock – Świerk, March 2015.

[39] C. Adolph et al. (COMPASS Collaboration), Phys. Lett. B **718**, 922 (2013).

[40] T. Szameitat, PhD thesis, University of Freiburg (2017), doi:10.6094/UNIFR/11686.

[41] A. Sandacz and P. Sznajder, "HEPGEN - generator for hard exclusive leptoproduction", (2012), arXiv:1207.0333.

[42] C. Regali, PhD thesis, University of Freiburg (2016), doi:10.6094/UNIFR/11449.

[43] E. Burtin, N. d'Hose, O.A. Grajek and A. Sandacz, "Angular distributions and $R = \sigma_L/\sigma_T$ for exclusive ρ^0 production", private communication.

[44] P. Söding, Phys. Lett. B **19**, 702 (1966).

[45] S. Brodsky et al., Phys. Rev. D **50**, 3134 (1994).

[46] L. Frankfurt, W. Koepf and M. Strikman, Phys. Rev. D **54**, 3194 (1996).

[47] S.V. Goloskokov and P. Kroll, Eur. Phys. J. C **50**, 829 (2007).

[48] L. Favart, M. Guidal, T. Horn and P. Kroll, Eur. Phys. J. A **52**, 158 (2016).